Rowan University

Rowan Digital Works

Theses and Dissertations

4-6-2021

Numerical modeling of the fiber deposition flow in extrusion-based 3D bioprinting

Dhanvanth Jaya Talluri
Rowan University

Follow this and additional works at: https://rdw.rowan.edu/etd

 Part of the Mechanical Engineering Commons

Recommended Citation

Talluri, Dhanvanth Jaya, "Numerical modeling of the fiber deposition flow in extrusion-based 3D bioprinting" (2021). *Theses and Dissertations*. 2877.
https://rdw.rowan.edu/etd/2877

This Thesis is brought to you for free and open access by Rowan Digital Works. It has been accepted for inclusion in Theses and Dissertations by an authorized administrator of Rowan Digital Works. For more information, please contact graduateresearch@rowan.edu.

www.manaraa.com

NUMERICAL MODELING OF FIBER DEPOSITION FLOW IN EXTRUSION-BASED 3D BIOPRINTING

by

Dhanvanth Jaya Surya Saran Talluri

A Thesis

Submitted to the
Department of Mechanical Engineering
College of Engineering
In partial fulfillment of the requirement
For the degree of
Master of Science in Mechanical Engineering
at
Rowan University

Thesis Chair: Amir K. Miri, Ph.D.

Committee Members:
Anu Ranjan Osta, Ph.D.
Trkov Mitja, Ph.D.

www.manaraa.com

© 2021 Dhanvanth Jaya Surya Saran Talluri

www.manaraa.com

Dedications

I would like to dedicate this work to my advisor Amir K. Miri, Ph.D., my parents, my friends and all the people who have supported me in my academic career.

www.manaraa.com

Acknowledgments

Apart from my efforts, this research project's success was due to many others' encouragement and guidance. I want to express my sincere gratitude to my principal advisor, Dr. Amir K. Miri, Assistant Professor of Mechanical Engineering, for his patience, motivation, support, and enthusiasm. I also thank my thesis committee members, Dr. Anu Osta and Dr. Mitja Trkov , Department of Mechanical Engineering. My notable thanks to Dr. Reza Avaz, Department of Mechanical and Biomedical Engineering, Texas A&M University, for providing his research work for my project and his technical support. My sincere thanks go to the Rowan University Department of Mechanical Engineering for providing me an opportunity to pursue my Master's degree with full financial support. I am especially indebted to my parents for their immense love and support. Finally, I would like to express my sincere thanks to my friends and colleagues, who have guided and encouraged me during my graduate studies at Rowan University.

www.manaraa.com

Abstract

Dhanvanth Jaya Surya Saran Talluri
NUMERICAL MODELING OF THE FIBER DEPOSITION FLOW IN EXTRUSION-BASED 3D BIOPRINTING
2019-2020
Amir K. Miri, Ph.D.
Master of Science in Mechanical Engineering

Extrusion bioprinting involves the deposition of bioinks in a layer-wise fashion to build 3D structures that mimic natural living systems' behavior in tissue engineering. Hydrogels are the most common bioinks, in which their viscosity properties are dependent on the shear-rate, such as Non-Newtonian fluids. Numerical simulation of extrusion bioprinting may help study the flow properties of hydrogels and designing improved bioinks. In this thesis, the instability caused by the shear-thinning or -thickening parameter during extrusion is numerically compared with the theoretical estimations. The process of fiber deposition of hydrogels onto a substrate through the single and coaxial nozzle is done using a commercial package (ANSYS Fluent). For various power-law bioinks, the morphology of single and multi-layer 3D bioprinted fibers, including the velocity, printing pressure, wall shear stress, and mixing proportion of two bioinks during bioprinting, are predicted for the first time.

www.manaraa.com

Table of Contents

www.manaraa.com

Table of Contents (Continued)

www.manaraa.com

List of Figures

www.manaraa.com

List of Figures (Continued)

Figure Page

www.manaraa.com

List of Figures (Continued)

Figure Page

www.manaraa.com

List of Tables

www.manaraa.com

Chapter 1

Introduction

1.1 Extrusion-Based 3D Bioprinting

Extrusion-based three-dimensional (3D) bioprinting, sometimes called direct writing [1], is a fabrication method by which hydrogels containing biomaterials/cells are deposited through a long and narrow extruder nozzle. The fibers are successively deposited on top of a substrate in a layer-wise fashion to build a 3D construct model containing living components. The displacement of the extrusion nozzle relative to the substrate can be controlled by the liquid hydrogel being deposited along with a predefined pattern. This approach is beneficial when bioprinting large cell concentrations to accelerate growth and tissue growth. But the possible detrimental effects on cell viability and functionality of polymerization and shear forces must be considered before the parameters of the bioprinting process are optimized. Shear-thinning behavior where resistance is decreased upon shear flow is required for an ideal bioink [2]. It should also be able to recover its mechanical properties relatively quickly upon exiting the nozzle. For biological applications, this technology seems ideal as it can deposit heterogeneous materials with a broad selection of properties. After printing, the scaffolds are normally soft, and they must be treated with some forms of gelation post-printing [3] to sustain their structural integrity. Tissue scaffolds are porous structures with interconnected architectures that promote cell metabolism by imitating the cellular environment, while offering sufficient mechanical support to preserve structure stability.

Based on the ejection process, extrusion bioprinting approaches can be divided into three groups (Figure 1): pneumatic-, piston-, and screw-based bioprinting [4]. Pneumatic

www.manaraa.com

bioprinting is a method of driving biomaterials/cells out of a syringe using compressed air at a controllable volume scale. The accuracy of the bioink deposition highly relies on its flow properties, which can be greatly influenced by the solution's dynamic viscosity [5]. In contrast, biomaterial/cell solutions are mechanically driven by a rotating screw-driven or linear piston moving alignment in piston- or screw-based bio-printing mechanisms [6]. Both printing systems may have strong deposition forces to monitor the volumes of the solution.

Figure 1

Common methods of deposition in extrusion-based bioprinting [7].

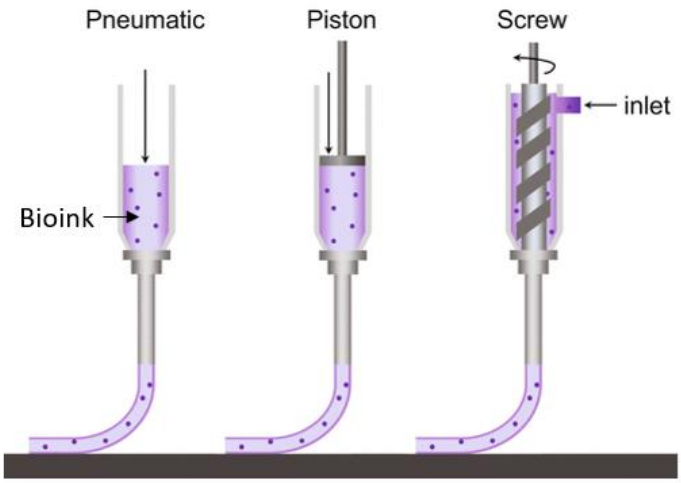

Mechanically driven systems involve relatively complex components and high driving forces [8]. A wide variety of viscous fluids are consistent with extrusion-based bioprinting. To provide structural support for tissue scaffolds, high viscous bioinks are

www.manaraa.com

more desirable, whereas low viscous bioinks are more suited for cellular bioactivity [9], [10]. Therefore, to ensure both the mechanical integrity of tissue scaffolds and cell functionality, the synthesis of materials with predicted flow behavior must be thoroughly investigated. Mechanical stability of constructs can be improved by dispensing dense bioink fibers or reducing porosity by managing the nozzle diameter or monitoring the bioprinting process. Yet, thicker fibers and lower porosities limit cell diffusion and restrict the exchange of nutrients and metabolic waste [11]. Decreasing the diameter of fibers, on the other hand, can remove diffusion barriers. As specific cell types need unique conditions, it is crucial to modify scaffolds' mechanical properties by controlling the bioink types, bioink viscosities, or the bioprinting process to fulfill structural stability and cellular functionality needs [12]. Another approach to monitoring use of multiple bioinks and bioink viscosities is co-axial extrusion bioprinting.

As a multi-material bioprinting method, coaxial bioprinting involves two separate layers of different biomaterials, cells, and cross-linking agents, in which the two layers are called “shell and core” (Figure 2A)[13]. Different combinations of biomaterials can simultaneously be extruded through the coaxial filament (Figure 2B) for better tissue regeneration ability. Coaxial bioprinting can have a synergistic effect on printability, structural complication, shape fidelity, and biocompatibility of two materials with different mechanical and biochemical properties. Generally, the high stiffness of bioinks may harm the biological activities of the encapsulated cells in them.

www.manaraa.com

Figure 2

A) Multi-layer bioprinted fiber, and B) Coaxial nozzle head [14].

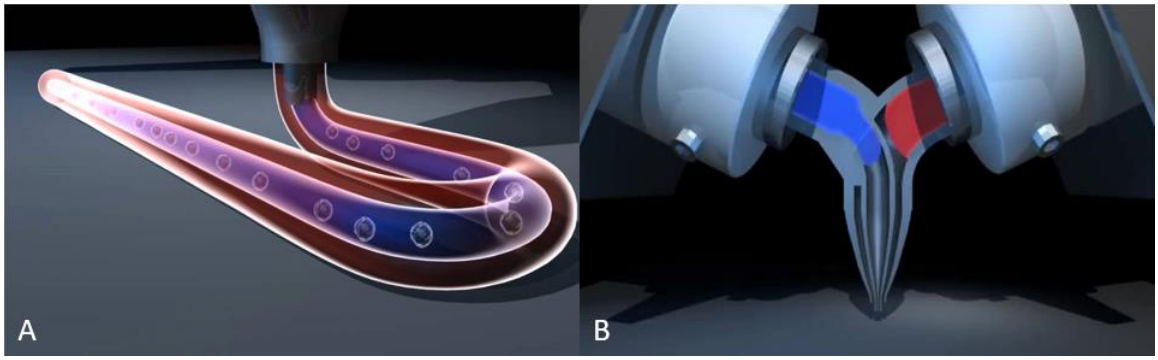

Bioinks with relatively weak mechanical properties can provide micro-environments suitable for cell viability and proliferation, but they do not produce well-built 3D structures. By enabling users to choose several biomaterials for specific uses, coaxial printing is a way to address the current limitations of bioprinting [15]. For example, a stiffer material may be used in the center for mechanical support, while a comparatively material of lower stiffness can be placed in the shell for biological activity. Coaxial bioprinting has tremendous potential for creating stable mechanical properties and biological activities in a clearly built structure. It is also broadly used to build hollow or tube-like structures [16]. Coaxial-printed tubular constructs can mimic natural vascular networks because of the ability to provide nutrients, oxygen, and other biochemical elements through the core part. In terms of biological events such as cell-scaffold association, adaptation, proliferation, and even angiogenesis from soft to hard tissues, the control of coaxial made scaffolds over single-nozzle printed scaffolds has recently been shown [15]. As a simple and effective method for acquiring desirable bioink properties, multi-material hydrogels are earning

www.manaraa.com

popularity. Multi-material bioinks have favorable printability and high structural fidelity due to their high viscosity and shear-thinning characteristics.

1.2 Bioinks

Bioinks are the materials for 3D bioprinting, and they may contain living cells (suspended or in aggregates) and extracellular matrix materials, such as suitable hydrogels, cell media, and other additives. Two major types of bioinks used for developing tissue/organ structures are: cell-scaffold based approach and scaffold-free cell-based approach [17]. In the first method, the bioink contains biomaterials/cells printed to develop 3D tissue constructs. The scaffold biodegradation occurs at this time, and the encapsulated living cells grow and occupy space to form pre-designed tissue constructs. In the other method, living cells are printed directly in a method that resembles natural cell proliferation. A preferred group of live cells forms neoplasm tissues, which are later accumulated in a particular arrangement to form a combination of large functional tissue structures over time [18]. For a cell-scaffold-based approach, the optimal bioink preparation should meet those biomaterial and biological requirements.

Biomaterial properties involve printability, mechanical characteristics, biodegradation, and maturation after bioprinting. Biological criteria primarily involve biocompatibility (not only non-toxic to other tissues/cells, but also the endurance of live cells inside bioink), cytocompatibility, and post-print bioactivity of cells. It is necessary to know the processing capabilities of the bioink formulation when the printability property of the bioinks is considered. After printing, it should also have the potential to self-hold

www.manaraa.com

the 3D printed structure. The printability of the bioink depends on several factors, such as the viscosity of the bioink solution, the surface tension of the bioink, its own cross-link ability, and the surface properties of the printer nozzle. The printing efficacy and the encapsulation of live cells have strongly relied on the bioink solution hydrophilicity and viscosity. If the bioink formulation is very viscous, the pressure needed for extrusion may be higher, and it will influence the flow of the polymer solution from the tiny nozzle orifice. Compared to lower viscous solution formulations, this high viscous solution can create 3D structures with greater stability[17]. The use of the same bioink in various commercially available bioprinters allows the properties of the bioink formulation to be tunable.

We beleive that the bioink instability immediately after leaving the nozzle is a crucial biophysical element in the extrusion-based bioprinting, showing how smoothly the bioink rests on the receiving substrate. Regarding extrusion-based bioprinting, bioink instability is characterized by any deviations from a constant curved cylinder over the surface of the paste-like filament. Instability also applies to a disturbance on a macro scale. Dynamic viscosity [19], yield stress, and the nozzle geometry are the major influencing properties for the onset instability of bioinks. The resistance of bioink to injection forces is indicated by viscosity, and it usually depends on the shear rate, i.e., non-Newtonian flow. It has also been stated that any decrease in yield stress facilitates the smoothness of bioink flow and surface distribution. The moderate yield stress was found to smooth the deposition process and maintain the shape, but high yield stress may lead to rapid moving of the fluid within the nozzle. By varying the printing velocity, bioink power-law coefficient, nozzle diameter, and nozzle height, we can precisely monitor instability at the deposition site.

www.manaraa.com

Shear-thinning or shear thickening behavior is one of the hydrogel's main features or any viscoelastic system [20]. All pseudoplastic hydrogels are shear thinning. In medicine, the ability of shear-thinning is highly developed for tissue engineering and drug delivery. A few peptides based, recombinant protein-based, colloidal, and blended hydrogels have been documented. They self-heal and thin out with an increasing shear rate and viscosity recovers when the shear-thinning is removed. Shear-thinning hydrogels have a high content of water and can be supplied in a minimally invasive way. If made of natural polymers, these hydrogels have the benefits of exceptional biocompatibility, lower toxicity, and decomposition costs. During self-supporting rapid solidification printing, bioink printability research focused primarily on the results of many primary factors, including bioink rheological features, bioink formulations, and operating conditions. The shear-thinning activity allows a pre-formed hydrogel to be delivered *in vivo* by applying shear stress during injection with desired physical properties, as characterized *ex vivo*. As the hydrogel is pre-formed *ex vivo*, the effect of the local environment on cross-linking is almost insignificant, whereas most injectable hydrogels are liquid before injection and can be affected by the *in vivo* environment during cross-linking. In shear-thinning hydrogels [21], the recovery of elastic modulus after shear can be much quicker than the gelation method of other forms of hydrogels. Finally, solely liquid precursor solutions can leak or dissolve with the body fluid into the surrounding tissue, which may restrict the development of hydrogel and pose questions about toxicity.

High precision during printing, *in situ* gelation, visco-elastic properties, low cost, easily available, industrial scalability, biomimicking of internal tissue structures, mechanical stability, limited post-printing time for maturation, and immunological

www.manaraa.com

viability when inserted *in vivo* and a wide variety of different cell types are other important desirable features for a bioink. Oxygen gas permeability, metabolic waste and the transport of nutrients are also essential. When choosing an excellent bioink material for 3D bioprinting, these fundamental criteria are very important. As described in the previous section, essential properties and features such as printability and mechanical properties, flexibility modifications, controlled biodegradability, and non-toxicity to cells (enable them to get their growth nutrients and further enhance their metabolic function during tissue regeneration) should be shown in the bioink specifications that are used in 3D bioprinting processes. Bioinks may be chosen according to the specifications of the desired tissues and organs and can be changed to regenerate the tissue or organ's appropriate structure.

1.3 Numerical Modeling

Fluids are a phase of matter that contain liquids and gases. They do not alter significantly under high stresses. Whereas solids resist applied shear or tangential stress by deformation, fluids flow under shear stress. While gases are fluids that fill their realms, liquids are fluids that shape a free surface in the presence of a gravitational force. Computational fluid dynamics (CFD) has made enormous strides [22], motivated primarily by the need of computer resources to address the CFD problem. Related mathematical equations can be interpreted and most of the equations used are extracted from concepts that are scientifically or experimentally valid and observed. The steps in applying a numerical solution are shown in Figure 3.

www.manaraa.com

Figure 3

Typical numerical analysis process [23].

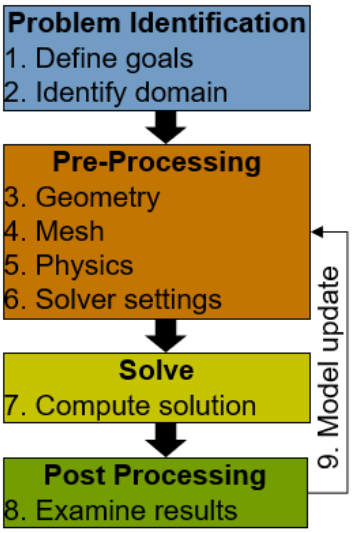

CFDs are commonly based on the Navier-Stokes equation, the diffusion (or heat) equation, and the Stokes-Einstein equation (representing the diffusivity of molecules depending on their size and affinity), but the Darcy and Brinkman equations that describe porous flow and more are required for extrusion bioprinting of hydrogels. It is challenging to model extrusion-based 3D printing because it requires multi-physical (thermal and dynamical) phenomena on various spatial and temporal scales: the extrusion of material is a local activity, whereas the manufacturing of an entire component is a global process. After the material deposition, previous modeling studies focused primarily on the printed component's thermal and thermal-mechanical behavior. The printed strand's local thermal background is measured by lumped capacitance analysis [24] using analytical and computational thermal models. Thermal models are also coupled with structure-based

www.manaraa.com

diffusion-driven models (driven by capillary forces) to predict the forming of a local bond between adjacent strands [25]. The entire component has been used as a global thermal-mechanical simulation to measure temperature-induced deformations before and after fabrication, and residual stresses within the final component, for its crystallinity and probable crack initiation sites. The material extrusion is usually emulated in these models by a thermal/thermo-mechanical finite-element or a threshold-volume solver activation technique. In the case of the global simulation and a generalized cylinder with oval, elliptical, or octagonal cross-sections in the local models, the geometry of the deposited strand is typically simplified by rectangular voxels. Thus, the shape of the strands is an important energy balance parameter: the strands exchange the heat through their interactions, while their free surfaces exchange heat through convection and radiation [26].

The detailed thermal models would be better analyzed through CFD simulations of deposition flow when the structure of extruded strand was determined. In a model developed by Ahn et al. [27], the principal parameters are the cross-section of the strands and their overlap time (necessary for healing). These parameters are used for parameter regression, which they require CFD simulations. The CFD simulations of the strand deposition can be used to predict the interstitial vacuum density between the strands directly in the mechanical behavioral models of the produced component. The CFD simulations presented in [28], [29] are for the non-isothermal power-law fluids inside the extruder's nozzle. The flow field within the extruded material, pressure drop inside extruders, and the melting distance from the liquefier injection shall be determined from these CFD simulations.

www.manaraa.com

Heller [30] used CFD calculations to measure the composite polymer's flow-inducing strand orientation inside a needle of Newtonian isothermal fluid using an axisymmetric extrusion needle. The effect of extruder geometry on the flow-induced pit orientation was studied; however, the deposition flow after the needle exit was not included in their CFD model. During deposition of the substance, McIlroy and Olmsted [31] have engineered an amorphous polymer's disintegration, expecting a smooth, detailed approach to the deposition flow, which avoids secondary flows. The deposition flow has been documented in condensed, two-dimensional simulations in [32]. The multiple strands positioned above each other by a high-precision 3D surface tracking algorithm and the Newtonian fluid model was simulated by Dabiri et al. [33]. However, this model did not solve the real extrusion flow, as in this mass conservation equation, the volumetric source term emulated material extrusion. In a recent work, which calls the non-isothermal fluxes of (non-Newtonian) shear-thinning fluids, the 3D extrusion and deposition flow of semi-molten material has only been simulated to the authors' cognizance. Although the grid resolution was very coarse, the simulations from Du et al. [34] were capable of reliably predicting the region of interaction between the neighboring strands for various speed ratio values and the thickness of the coating. They have simulated molten metal deposition movement on a fusion-based AM basis using their computational models [35].

A significant parameter for the configuration of the liquefier and the feeding mechanism of the printing head is the overall drop in the pressures inside the extruder. Deficient operational conditions can result in a feedstock filament buckling or filament feedstock slippage on the feeding roller [36], [37], resulting in volumetric flow irregularities. In the idealized geometry of the extruder containing cylindrical and conical

www.manaraa.com

sections, Bellini et al. [38] suggested the mathematical model relating to the extrusion flux of liquefier hot flow and feeding roller mechanism (assuming no buckling or slipping of the feedstock filament) by analytical expression of non-isothermal fluid power-law flows. Abnormal fluid conditions (e.g., nozzle obstruction, overflow, fluid disruption, etc.) were suggested to be observed in dynamical extruder simulation from the vibrations of the accelerometers recorded in the printing head [39], [40]. However, these dynamic models ignore the printing force applied to the substrate by the extruded material, ignoring the fact that it also adds to the dynamics of the printing head [39].

Little research has been performed on modeling hydrogel fibers (3D bioprinting) and rheology of hydrogels used as feedstock [41], while a major amount of research was carried out on 3D printing [42], [43]. In this thesis, we present a 3D numerical model for the deposition of non-Newtonian fluid fibers projecting various hydrogels onto a substrate during and post 3D bioprinting process using a commercial CFD package (ANSYS Fluent). The variations in fiber profile with respect to the changes in the shear-thinning parameter were previously developed using theoretical model by Avaz et al., The nozzle diameters and nozzle heights for specific power-law fluids were chosen [45]. They are used to simulate multi hydrogel deposition through both single and double-nozzle nozzles by flowing different hydrogels individually or simultaneously to replicate the tubular and core-shell structures. The strand and velocity profiles of all power-law indices were compared to validate the model. This model will allow us to change the onset of instability by changing the bioink power-law index. By adjusting the bioink power-law coefficient and the nozzle diameter, we can precisely handle the instability at the deposition site. We illustrated how the shear-thinning or thickening of the bioink can control the stiffness of

www.manaraa.com

deposition and help choose the right parameters like nozzle diameter, power-law index for bioink to perform the 3D model of the bioprinting process. In the last part of this thesis, we introduced a new application of our tool in 3D bioprinted organoid models.

www.manaraa.com

Chapter 2

Theory

2.1 Introduction

Focusing on the macroscopic scale in the study of fluid flow phenomena [46], [47]. It is often believed that the fluid is a continuum so that its physical and flow characteristics are described as equivalent at any point in space. Fluid flow activity may be classified as either Newtonian or non-Newtonian. Newtonian fluids are characterized by a linear association between shear stress and shear rate, with molecular viscosity one, which is a measure of a fluid capacity to resist deformation subjected to stress, representing the slope of the linear function. For non-Newtonian fluids, this relation is nonlinear. Likewise, fluid flow can be divided into different types, such as one-dimensional or multi-dimensional, single-phase, or multi-phase, real or ideal, compressible or incompressible, turbulent or laminar, steady or unsteady, and rotational or irrotational. These classifications are intended to simplify the theoretical and modeling method of fluid flow phenomena.

Mathematically, flows are often graded according to the partial differential equations defining them. For example, in two individual variables, second-order partial differential equations are categorized as elliptic, hyperbolic, or parabolic [48]. Data moves along two characteristic lines in these equations, which can be real and distinct, real and coincident, or complex, relying on whether they are hyperbolic, parabolic, or elliptic. These different equation forms are solvable using computational methods. The fluid flows are governed by the Navier-Stokes equations, which are strongly nonlinear second-order partial differential equations in four independent variables. In general, the flows are

www.manaraa.com

unsteady and 3D. Similar terminology is used in their classification as they share various properties describing second-order equations in two individual variables. Recirculating flows are elliptic, Transient, and supersonic flows are hyperbolic, and boundary layer flows are parabolic. As flows may be subsonic in a specific portion of the domain and supersonic in other sections or viscous dominated near to walls and inviscid in the core area, it is tough to describe a flow as coming under one of the above three types and if it is of the mixed type. This classification is done into the following: parabolic flows that are influenced by upstream locations only, hyperbolic flows assisting discontinuities, and elliptic flows by both upstream and downstream locations in the solution.

2.2 Finite Volume Method

The Finite Volume Method (FVM) is a computational method that transforms the partial differential equations describing conservation laws into independent algebraic equations over finite volumes over differential volumes (or elements or cells). In a similar way to the finite difference or finite element system, the first step in the solution process is the discretization of the geometric domain, which is discretized into non-overlapping elements or finite volumes in the FVM. The partial differential equations are then discretized/transformed into algebraic equations by integrating them over each discrete variable. To compute the dependent variable values for each of the components, the system of algebraic equations is then solved. In CFD, the success of the FVM [49], [50] derives from the high versatility it gives as a method of discretization.

www.manaraa.com

Although the finite difference [51], [52], and finite element methods [53] have preceded it for many years, the Finite Volume Method played a leading role in the fluid flow simulation problems and correlated transport phenomena as a result of the effort carried out in the early 70s by the CFD group at Imperial College under the leadership of Professor Spalding [54], with contributors such as Patankar [55], Gosman [56]. The FVM owes much of its flexibility and success, that discretization takes place directly in the real space without translation amongst the physical coordinate system and the computational coordinate system being required. Moreover, the use of a collocated arrangement [57] made it ideal for the resolution of flows in complicated geometries. These advancements have expanded the applicability of the FVM to cover a wide range of applications while retaining the simplicity of its mathematical formulation. Another important characteristic of the FVM is that its numerics mirror the physics and conservation principles it models, such as the integral property of the governing equations and the properties of the terms it discretizes. From what follows, the semi-discretized form of an overall scalar equation is obtained. Then, along with some guiding principles, the properties needed by the method of discretization are discussed. The chapter ends with a study of a number of FVM-related subjects. The semi-discretized equation's transformation into algebraic equations would be the topic of a number of chapters to come.

2.2.1 Eulerian and Lagrangian Description of Conservation Laws

The conservation theory notes that such physical measured quantities be conserved over a local environment for an isolated system. This theory of conservation, or conservation law, is an axiom that cannot be mathematically proved but can be conveyed by a mathematical relationship. Various physical quantities such as mass, momentum, and

www.manaraa.com

energy are regulated by laws of this kind (i.e., the Navier-Stokes equations). Following either a Lagrangian (material volume, MV) or an Eulerian (control volume, CV) approach [58], the conservation laws concerning fluid flow and associated transfer phenomena can be mathematically formulated. In the Lagrangian flow field description (Figure 4A), the fluid is subdivided into parcels of fluid, and each parcel of fluid is tracked as it passes through space and time. These parcels are labeled using a time-independent position vector field x_0, generally chosen to be the parcels' center of mass at some initial time t_0, and the flow is termed by a function $x(t, x_0)$. The path line portrayed by a fluid parcel (Figure 4A) is obtained as the collection of spots occupied at different times.

On the other hand, as time progresses, the Eulerian solution (Figure 4B) focuses on particular positions in the flow region. Thus, the flow variables are functions of position x and time t, and the flow velocity is given by $v(t, x)$. As the derivative of the position of a fluid parcel x_0 with respect to time represents its velocity, the two specifications are related by

$$v\big(t, x(x_0, t)\big) = \frac{\partial}{\partial t} x(t, x_0) \qquad \text{(Eq.2.1)}$$

Changes in the properties of a flowing fluid may be determined either at a fixed point in space as fluid particles cross it (Eulerian) or by following a fluid parcel along its direction, depending on the above definition (Lagrangian).

www.manaraa.com

Figure 4

A) Lagrangian and B) Eulerian specification of the flow field [59].

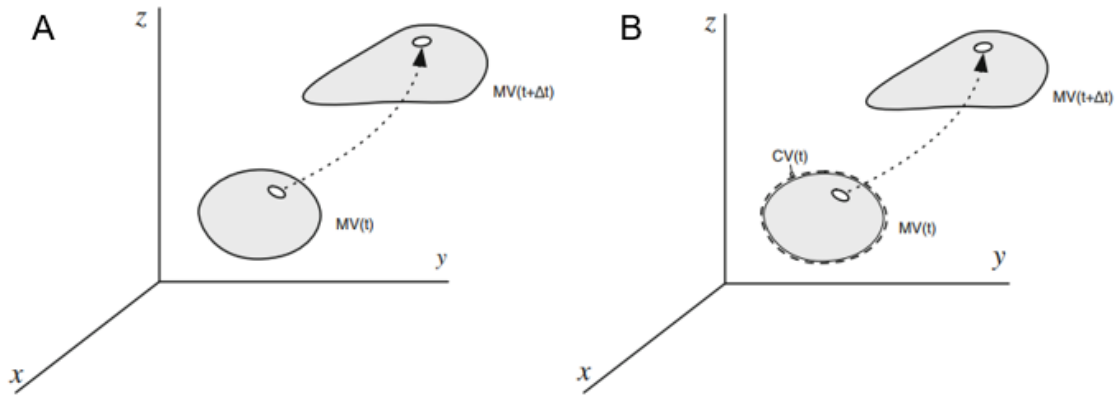

2.2.2 Reynolds Transport Theorem

For moving material volumes of fluids (Figure 4), and not for fixed points or control volumes, the conservation laws described above apply. There is a need to know the Eulerian equivalent to an integral taking over a moving material volume of fluid in order to express these laws according to a Eulerian approach. This is given by the transport theorem of Reynolds [60]. Depending on whether the control volume is constant, moving, or deformable, the conversion formula varies slightly. To derive the formula, let B be any property of the fluid (mass, momentum, energy, etc.) and let $b = dB/dm$ be the concentrated value of B (amount of B per unit mass) in any tiny element of the fluid.

For the random moving and deforming control volume shown in (Figure 4), the instantaneous total change of B in the material volume (MV) is equal to the instantaneous total change of B in the control volume (CV) plus the net movement of B into and out of

www.manaraa.com

the control volume through its control surface (S). Let ρ indicates the density of the fluid, n the outward normal to the control volume surface, $v(t,x)$the velocity of the fluid, $v_s(t,x)$ the velocity of the deforming control volume surface, and $v_r(t,x)$ the relative velocity by which the fluid enters/leaves the control volume [i.e., v_r=$v(t,x)$-$v_s(t,x)$], then the Reynolds transport theorem gives

$$\left(\frac{\partial B}{\partial t}\right)_{MV} = \frac{d}{dt}\left(\int_{V(t)} b\rho\, dV\right) + \int_{S(t)} b\rho v_r \,.n\, dS \qquad \text{(Eq.2.2)}$$

For a stable control volume, $v_s = 0$, and the geometry is time-independent, indicating that the time derivative term on the right-hand side of Eq. (2.2) can be written using the Leibniz rule as

$$\frac{d}{dt}\left(\int_V b\rho\, dV\right) = \int_V \frac{\partial}{\partial t}(b\rho)\, dV \qquad \text{(Eq.2.3)}$$

Therefore Eq. (2.2) simplifies to

$$\left(\frac{\partial B}{\partial t}\right)_{MV} = \int_V \frac{\partial}{\partial t}(b\rho)\, dV + \int_S b\rho v \,.n\, dS \qquad \text{(Eq.2.4)}$$

Applying the divergence theorem to convert the surface integral into a volume integral, Eq. (2.4) becomes,

www.manaraa.com

$$\left(\frac{\partial B}{\partial t}\right)_{MV} = \int_V \left[\frac{\partial}{\partial t}(\rho b) + \nabla \cdot (\rho v b)\right] dV \qquad \text{(Eq.2.5)}$$

An alternative form of Eq. (2.5) can be obtained by developing the second term in the square bracket and using the substantial derivative to get

$$\left(\frac{\partial B}{\partial t}\right)_{MV} = \int_V \left[\frac{D}{Dt}(\rho b) + \rho b \nabla \cdot v\right] dV \qquad \text{(Eq.2.6)}$$

Equation (2.5) or (2.6) can be used to derive the Eulerian form of the conservation laws in fixed regions.

Reynolds Number: The Reynolds number (Re) [61], [62] is defined as

$$Re = \frac{\rho U L}{\mu} \qquad \text{(Eq.2.7)}$$

And maybe understood as a measure of the relative importance of advection (inertia) to diffusion (viscous) momentum fluxes. If the momentum fluxes are in the same direction, the Reynolds number shows the characteristics of the flow's boundary layer. If the fluxes are described so that the diffusion is in the direction of the cross-stream, then, as seen in (Figure 5), *Re* conveys the regime of flow (i.e., laminar, transitional, or turbulent).

www.manaraa.com

Figure 5

Flow over a flat plate diagram showing the laminar, transitional, and turbulent flow regimes dependent on the value of Re [59].

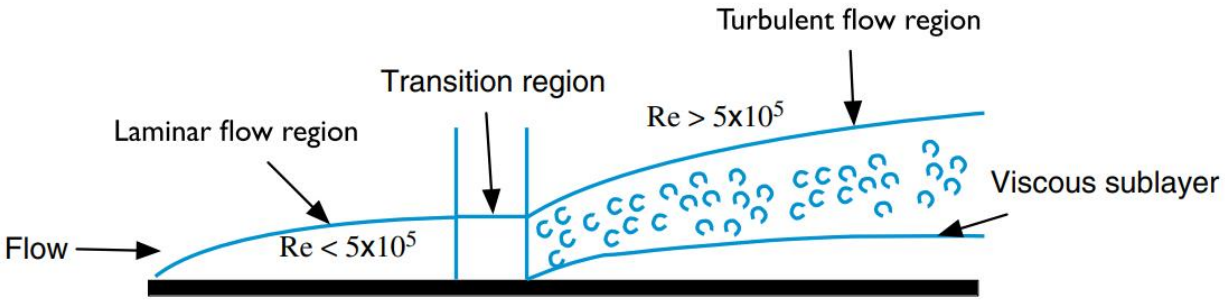

2.2.3 Conservation of Mass

The principle of conservation of mass [51], [52], [55]–[57] shows that in lack of mass sources and sinks, a region will conserve its mass on a regional level. Consider the material volume of fluid shown in (Figure 6) of mass m, density ρ, and velocity v, mass conservation in material (Lagrangian) coordinate system can be written as

$$\left(\frac{dm}{dt}\right)_{MV} = 0 \qquad \text{(Eq.2.8)}$$

For B = m, the corresponding intensive quantity is b = 1, and based on Eq. (2.6), the corresponding expression of mass conservation in an Eulerian coordinate system is

$$\int_V \left[\frac{D\rho}{Dt} + \rho\nabla \cdot v\right] dV = 0 \qquad \text{(Eq.2.9)}$$

www.manaraa.com

Figure 6

Conservation of mass for a material volume of a fluid of mass m [59].

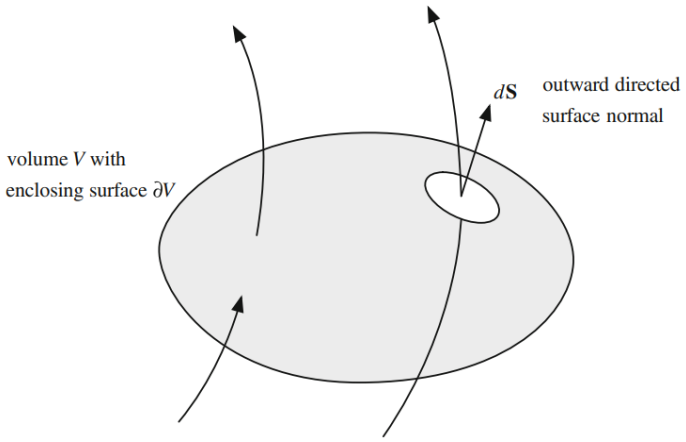

For the integral given in Eq. (2.9) to be accurate for any control volume V, the integrand must be equal to zero, providing the differential form of the mass conservation or continuity equation as

$$\frac{D\rho}{Dt} + \rho\nabla \cdot v = 0 \qquad \text{(Eq.2.10)}$$

The flux form of the continuity equation can be derived using Eq. (2.5) and leading to

$$\int_V \left[\frac{\partial\rho}{\partial t} + \nabla \cdot (\rho v)\right] dV = 0 \qquad \text{(Eq.2.11)}$$

www.manaraa.com

Again, for the integral in Eq. (2.11) to be accurate for any control volume V, the integrand must be equal to zero, providing the differential form of the mass conservation or continuity equation as

$$\frac{\partial \rho}{\partial t} + \nabla \cdot (\rho v) = 0 \qquad \text{(Eq.2.12)}$$

In the absence of any significant absolute pressure or temperature changes, it is acceptable to assume that the flow is incompressible; that is, the pressure changes do not significantly affect density. This is invariably the case in liquids and is a good approximation in gases at speeds considerably less than that of sound. Noting that sound waves are compressible phenomena. The most critical consequence in fluid dynamics is that the mass conservation equation can no longer be used to compute the density. The incompressibility condition indicates that q does not change with the flow, which mathematically can be expressed as $D\rho/Dt = 0$. Applying the mass conservation equation given by Eq. (2.10), this is equivalent to stating that the continuity equation for incompressible flow is given by

$$\nabla \,.\, v = 0 \qquad \text{(Eq.2.13)}$$

or in integral form as

$$\int_S (v \,.\, n)\, dS = 0 \qquad \text{(Eq.2.14)}$$

www.manaraa.com

Equation (2.14) says that for incompressible flows, the net flow throughout any control volume is zero, i.e., “flow out” = “flow in.”

Also, note that $D\rho/Dt = 0$ does not imply that ρ is the same everywhere (although this happens to be the case in many hydraulic applications), but that ρ does not change along a streamline. To be exact, the incompressibility approximation suggests that every single fluid element keeps its original density as it moves. In practice, density differences are commonly encountered in water due to variation in salt concentration and in the air due to temperature differences resulting in important buoyancy forces.

2.2.4 Conservation of Momentum

The principle of conservation of linear momentum [58], [60], [63]–[65] suggests that in the absence of any external force acting on a body, the body maintains its overall momentum, i.e., the product of its mass and velocity vector. Momentum being a vector quantity, its components are often conserved in any direction. In respect of a substance's material volume, Newton's Second Law of Motion states that only in the presence of a net force on that substance, like surface forces and corps forces, the momentum of this defined volume will change. Hence, by considering the material volume of fluid shown in (Figure 7) of mass m, density ρ, and velocity v, Newton’s Second Law in Lagrangian coordinates can be written as

$$\left(\frac{d(mv)}{dt}\right)_{MV} = \left(\int_V f\, dv\right)_{MV} \qquad \text{(Eq.2.15)}$$

www.manaraa.com

Figure 7

Conservation of linear momentum for a material volume of a fluid of mass m [59].

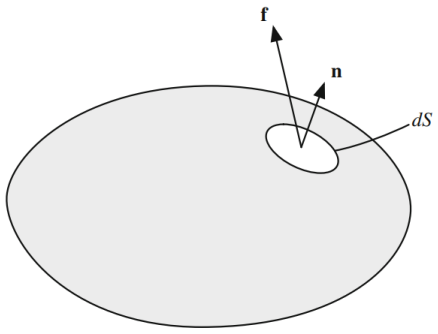

where f is the external force per unit volume acting on the material volume. The right-hand side of Eq. (2.15) is an integral volume over material coordinates carried out over the volume instantaneously filled by the moving fluid, thus

$$\left(\int_V f\, dV\right)_{MV} = \int_V f\, dV \qquad \text{(Eq.2.16)}$$

The equivalent expression of Eq. (2.15) in Eulerian coordinates can be written in two ways, known as the conservative and non-conservative forms.

Non-Conservative Form: Noticing that in this case $b = v$, the non-conservative form is obtained by using Eq. (2.6) in the derivation yielding

www.manaraa.com

$$\int_V \left[\frac{D}{Dt}[\rho v] + [\rho v \nabla \cdot v] - f\right] dV = 0 \qquad \text{(Eq.2.17)}$$

For the integral to be zero over any control volume, the integrand must be zero. Thus,

$$\frac{D}{Dt}[\rho v] + [\rho v \nabla \cdot v] = f \qquad \text{(Eq.2.18)}$$

Expanding the material derivative of the momentum term and reorganizing, the non-conservative form is obtained as

$$\rho \frac{Dv}{Dt} + v\left(\frac{D\rho}{Dt} + \rho \nabla \cdot v\right) = f \qquad \text{(Eq.2.19)}$$

$$\left(\frac{D\rho}{Dt} + \rho \nabla \cdot v\right) \; is \; Continuity$$

Using the continuity constraint and expanding the material derivative, the non-conservative form of the momentum equation reduces to

$$\rho\left(\frac{\partial v}{\partial t} + (v.\nabla)v\right) = f \qquad \text{(Eq.2.20)}$$

Conservative Form: The conservative version is obtained by applying the form of the Reynolds transport theorem given by Eq. (2.5) and is written as

www.manaraa.com

$$\int_V \left[\frac{\partial}{\partial t}[\rho v] + \nabla.\{\rho vv\} - f\right] dV = 0 \qquad \text{(Eq.2.21)}$$

By setting the integrand to zero for the integral to be zero for any volume V, the conservative form of the momentum equation is obtained as

$$\frac{\partial}{\partial t}[\rho v] + \nabla.\{\rho vv\} = f \qquad \text{(Eq.2.22)}$$

Where ρvv is the dyadic product.

Both types can help explain the concepts of discretization and demonstrate actual details of implementation. The conservative form will be added in the derivations that follow. By invoking the continuity constraint, the non-conservative form can be easily obtained from the conservative form at any point.

Once the external surface and body forces acting on the control volume are defined, the momentum equation's full form is obtained. The force f is separated into two one denoted by f_s representing the surface forces and the second by f_b representing the body forces such that

$$f = f_s + f_b \qquad \text{(Eq.2.23)}$$

www.manaraa.com

2.3 Domain Discretization

A computational mesh (Figure 8) on which the governing equations are subsequently solved is created by the discretization of the physical domain or mesh generation. Over the last few decades, the methods and techniques used for domain discretization have evolved drastically [66], [67] and have been largely automated [68]–[71]nowadays. The features and characteristics that the mesh system should possess to be used in the sense of the finite volume approach are first defined before evaluating the types of elements typically used in a computational mesh. In calculating the gradient of a vector φ on both a structured and unstructured triangular mesh, these attributes will be provided. Generally, using either a structured or an unstructured grid scheme, a geometric domain can be discretized. The 3D elements are defined by their local indices in a structured mesh (i, j, k). There are several coding and performance benefits to a structured grid system, but it suffers from limited geometric flexibility.

Additional complexity can be achieved in the generation of structured meshes by using multiple blocks to describe the geometry, with a structured mesh created either independently or jointly for each block. Another approach to make the generation of the mesh more flexible is to avoid the use of structured grids with their implicit topological information and to implement an unstructured mesh based on connectivity tables and geometric entity numbering with explicit topological information. For a long time, standardized grids have remained the staple of numerical modeling, and unstructured grids have only become more popular in the past two decades [72]. As problem size grew and manual mesh generation became too time-consuming [68], an automatic mesh generation was used from the early 1970s and onward. The first methods were semi-automatic, with

www.manaraa.com

an operator manually putting points in the computational domain and then using a computer to create the mesh in a second stage. Nowadays, with all points and elements created automatically, the whole process is completely automated. In addition to several hybrid multi-block grids [73], most modern CFD codes can use unstructured grids. Open FOAM software [74] uses unstructured grids and can also use multi-block grids that are conforming and non-conforming [75]. In the background of an unstructured grid system, the finite volume method will be discussed here. However, its characteristics can be compared to those of a structured grid system as the unstructured finite volume mesh specifications are specified.

Figure 8

A) Domain of interest, B) Domain discretized using a uniform grid system, C) Domain discretized using an unstructured grid system with triangular elements [59].

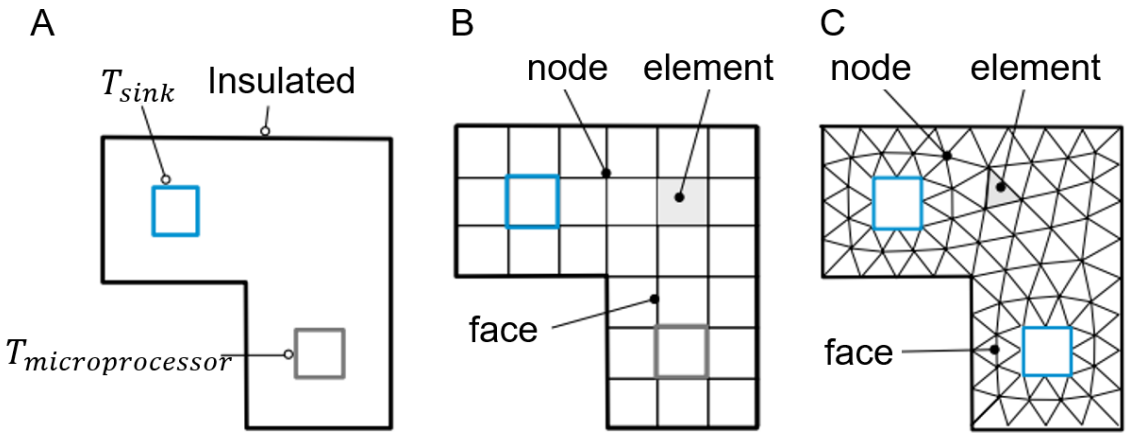

www.manaraa.com

2.3.1 The Finite Volume Mesh

Each interior cell in the domain is connected to the same number of neighboring cells for a regular structured grid. These adjacent cells (Figure 9) can be defined using the indices i, j, and k) respectively in the direction of the x, y, and (z) coordinates and can be reached directly by incrementing or decrementing the corresponding indices. Because topological information is embedded in the mesh structure via the indexing mechanism, enabling lower memory use. This also contributes to more excellent coding, cache utilization, and vectorization efficiency. In the development of the Finite Volume and Finite Difference methods, structured grids were commonly used. In a structured grid, an ordered set of indices (i, j, k) can be associated with each computational cell, where each index differs over a fixed range, regardless of the values of the other indices, and where adjacent cells have associated indices differing by plus or minus one. Thus, if there are elements Ni, Nj, and Nk in the index direction of i, j and k, respectively, then Ni *Nj* Nk is the total number of elements in the domain. Elements are hexagons with six faces and eight vertices in 3D spaces, with each interior element having six neighbors. Elements are quadrilaterals with four faces and four vertices in two dimension, with four neighbors for each interior element.

www.manaraa.com

Figure 9

Local indices and topology for a structured mesh [59].

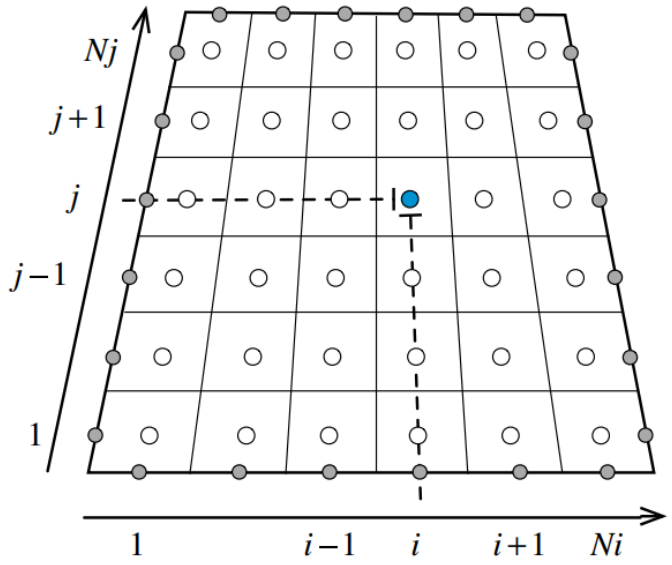

In meshing an area, unstructured grids provide more consistency in terms of all the element forms used and in terms of where the elements can be concentrated. However, this stability comes at the expense of additional complexity. Elements are sequentially numbered in an unstructured mesh system, as are faces, nodes, and other geometric quantities. This suggests that, based on their indexes alone, there is no direct way to connect different entities together. Local connectivity must then be clearly specified, beginning with the determination of geometric quantities for a specific element. Just in (Figure 10), The neighbors of element 9, for instance, cannot be directly taken from its index. Likewise, the bounding faces of element 9, or their nodes, cannot be calculated or extracted from its index in the same manner as this can be achieved in a structured grid. Therefore, detailed

www.manaraa.com

topological information about neighboring elements, faces, and nodes is needed to complement the grid's global indexing.

Figure 10

Unstructured mesh global indexing [59].

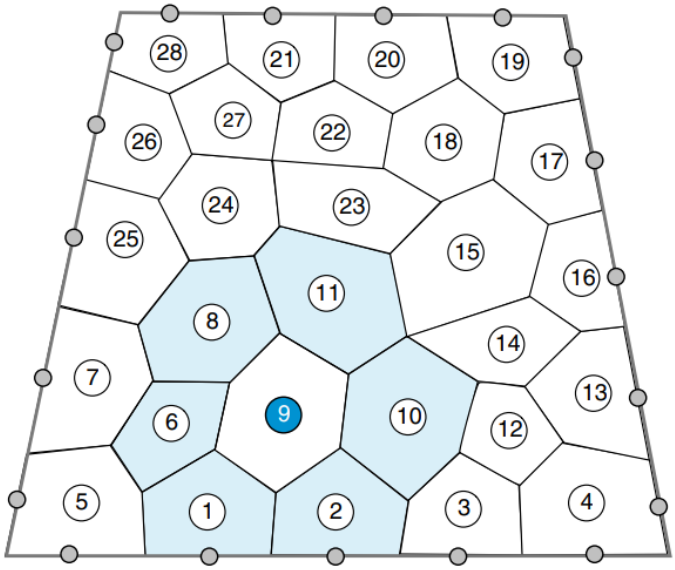

2.3.2 Element Types

The finite volume mesh element is essentially a 3D mesh polyhedron (Figure 11) or a two-dimensional mesh polygon (Figure 12). The 3D shapes that are most used, as seen in (Figure 11), tetrahedrons, hexahedrons, prisms, and general polyhedrons in some situations. The type of faces for these 3D elements, which often represent the type of two-dimensional elements (Figure 12), varies greatly, with quadrilaterals, triangles, and

www.manaraa.com

pentagons being the most used. At the same time, some applications have also used general polygons.

Figure 11

Three-dimensional (3D) element types [59].

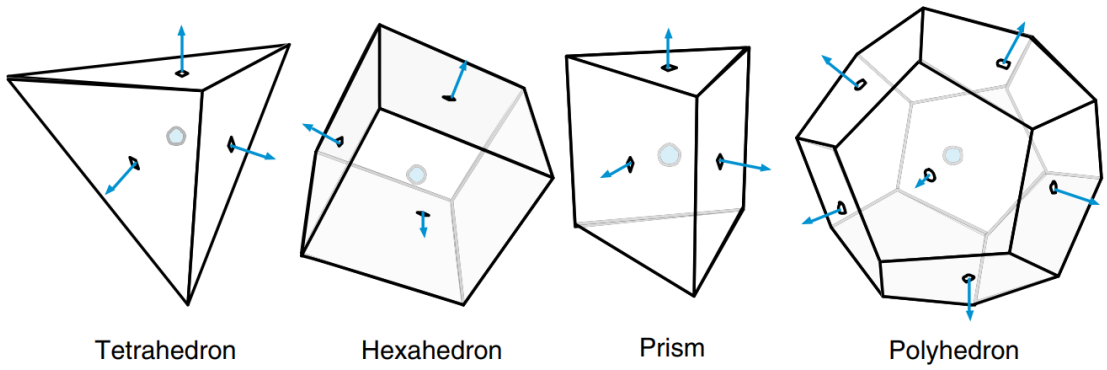

www.manaraa.com

Figure 12

Three-dimensional (3D) face types or two-dimensional element types [59].

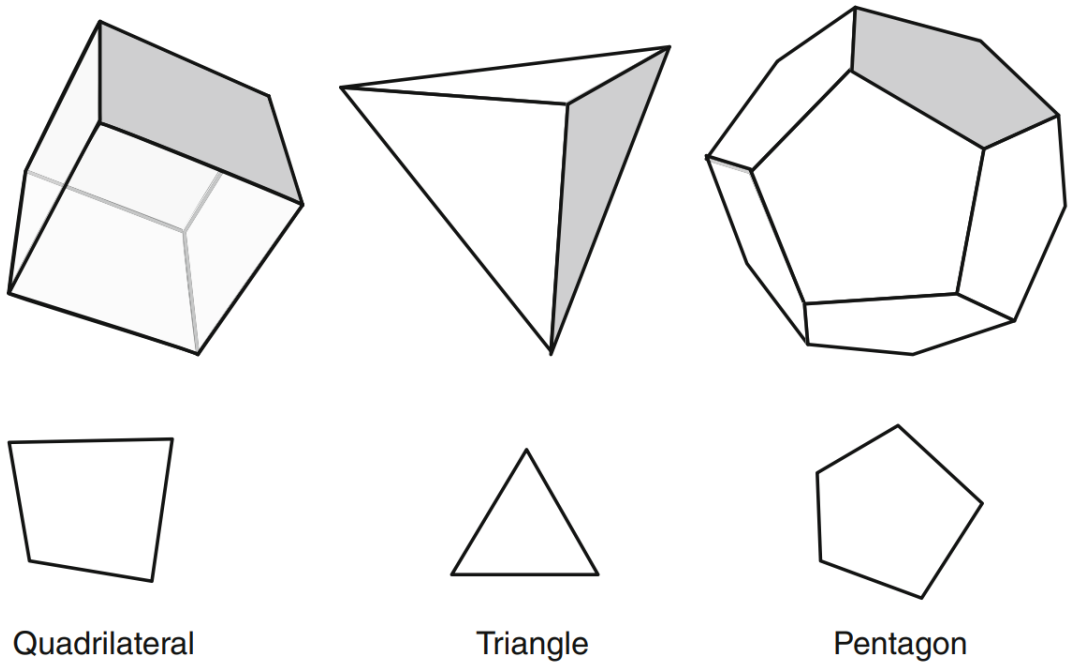

For such elements and faces, the computation of geometric factors can now be detailed. Interestingly, the volume of the elements is assumed to be the area of the two-dimensional elements multiplied by a unit dimension in the off-plane direction when dealing with a two-dimensional mesh. Thus, the methods used to measure the volume of two-dimensional mesh elements are specifically those used to calculate the surface area of 3D mesh faces. When necessary, other variables arising during discretization will be presented, which are solely dependent on geometric quantities.

www.manaraa.com

The theory of fluid mechanics, derived from observed physical principles, was accompanied by CFD. This section includes the calculations that are most relevant and used in the estimation. Inherent in these thoughts is ANSYS Fluent [76], part of the ANSYS Workbench 2020 R1, in the program kit used. ANSYS Fluent is an efficient, customizable CFD tool with geometry, material properties, flow profiles, and reaction speeds, all important to the simulated model specification. As a mathematical model with improperly formalized parameters, it is necessary to consider the equations applied or dealt with that would have an inaccurate and most likely irrelevant solution that will prevent testing due to the lack of practical experimental implementation.

2.4 Fluent Model

A significant number of flows found in nature and science is a combination of phases. Gas, liquid, and solid are physical phases of matter, but the phase principle is used as an identifiable material class with a clear inertial response to and contact with the flow in which it is immersed. For example, since each set of particles of the same size would have a similar dynamic reaction to the flow field, different-sized solid particles of the same substance may be viewed as distinct phases.

VOF Model (Multiphase Model): Through solving a single set of momentum equations and tracing the volume fraction of each of the fluids in the domain, the VOF model will model two or more immiscible fluids [76].

By using either the Euler-Lagrange method or the Euler-Euler approach, multi-phase flows can be measured numerically. VOF is a type of approach to Euler-Euler,

www.manaraa.com

essentially a technique of surface monitoring. Commonly used where there are more than two immiscible fluids, where the interface's location is significant.

It only has one series of momentum equations, shared by all fluids, and each fluid's volume fraction is tracked in each computational cell. The equation of momentum, seen below, relies on the fractions of the volume of all phases by the properties of ρ and μ.

$$\frac{\partial}{\partial t}(\rho\vec{v}) + \nabla \cdot (\rho\vec{v}\vec{v}) = -\nabla_p + \nabla \cdot [\mu(\nabla\vec{v} + \nabla\vec{v}^T)] + \rho\vec{g} + \vec{F} \qquad \text{(Eq.2.24)}$$

Volume Fraction Equation: The control of the interface(s) between the phases is achieved by using a continuity equation for a fraction of one or more of the phases. This equation has the following form for the q^{th} phase [76].

$$\frac{1}{\rho_q}\left[\frac{\partial}{\partial t}(\alpha_q\rho_q) + \nabla \cdot (\alpha_q\rho_q\vec{v}_q) = S_{\alpha_q} + \sum_{p=1}^{n}(\dot{m}_{pq} - \dot{m}_{qp})\right] \qquad \text{(Eq.2.25)}$$

where $\dot{m}_{qp}$ is the mass transfer from phase **q** to phase **p** and $\dot{m}_{pq}$ is the mass transfer from phase **p** to phase **q**. By default, the source term on the right-hand side of the above Equation, S_{α_q}, is zero, but you can specify a constant or user-defined mass source for each phase.

www.manaraa.com

The Implicit Scheme

$$\frac{\alpha_q^{n+1}\rho_q^{n+1} - \alpha_q^n \rho_q^n}{\Delta t} V + \sum_f \left(\rho_q^{n+1} U_f^{n+1} \alpha_q^{n+1}, f\right) = \left[S_{\alpha_q} + \sum_{p=1}^{n} \left(\dot{m}_{pq} - \dot{m}_{qp}\right)\right] V \quad \text{(Eq.2.26)}$$

The Explicit Scheme

$$\frac{\alpha_q^{n+1}\rho_q^{n+1} - \alpha_q^n \rho_q^n}{\Delta t} V + \sum_f \left(\rho_q U_f^n \alpha_q^n, f\right) = \left[S_{\alpha_q} + \sum_{p=1}^{n} \left(\dot{m}_{pq} - \dot{m}_{qp}\right)\right] V \quad \text{(Eq.2.27)}$$

Where

n+1 = index for new (current) time step

n = index for previous time step

α_q, f = face value of the q^{th} volume fraction, computed from the first- or second-order upwind, QUICK, modified HRIC, compressive, or CICSAM scheme

V = volume of cell

U_f = volume flux through the face, based on normal velocity

Viscosity for Non-Newtonian Fluids [77]: For incompressible Newtonian fluids, the shear stress is proportional to the rate-of-deformation tensor $\overline{\overline{D}}$:

www.manaraa.com

$$\bar{\bar{\tau}} = \mu\bar{\bar{D}} \quad \text{(Eq.2.28)}$$

where $\bar{\bar{D}}$ is defined by

$$\bar{\bar{D}} = \left(\frac{\partial u_j}{\partial x_i} + \frac{\partial u_i}{\partial x_j}\right) \quad \text{(Eq.2.29)}$$

and μ is the viscosity, which is independent of $\bar{\bar{D}}$.

For some non-Newtonian fluids, the shear stress can similarly be written in terms of a non-Newtonian viscosity η:

$$\bar{\bar{\tau}} = \eta(\bar{\bar{D}})\bar{\bar{D}} \quad \text{(Eq.2.30)}$$

In general, η is a function of all three invariants of the rate-of-deformation tensor $\bar{\bar{D}}$. However, in the non-Newtonian models available in ANSYS FLUENT, η is a function of the shear rate $\dot{\gamma}$ only. $\dot{\gamma}$ is related to the second invariant of $\bar{\bar{D}}$ and is defined as

$$\dot{\gamma} = \sqrt{\frac{1}{2}\bar{\bar{D}}:\bar{\bar{D}}} \quad \text{(Eq.2.31)}$$

Power Law for Non-Newtonian Viscosity

$$\eta = k\dot{\gamma}^{n-1}H(T) \quad \text{(Eq.2.32)}$$

www.manaraa.com

where ***k*** and ***n*** are inputs. ***k*** is a measure of the fluid's average viscosity (the consistency coefficient); ***n*** is a measure of the fluid's divergence from the Newtonian (the power-law index); $H(T)$ known as the Arrhenius law for the fluids where the viscosity also depends on temperature. The value of **n** shall decide the class of the fluid:

$n = 1 \rightarrow$ Newtonian fluid

$n > 1 \rightarrow$ shear-thickening (dilatant fluids)

$n < 1 \rightarrow$ shear-thinning (pseudo-plastics)

www.manaraa.com

Chapter 3

Role of Shear-Thinning

3.1 Introduction

In this chapter, Avaz et al., investigated the behavior of bioink on the threshold of instability using a power-law fluid suspension model (with rigid particles as a simple model of encapsulated cells). This theoretical model may enable the ability to tune the onset of instabilities by altering the concentration of the rigid particles. In practice, the instabilities at the deposition site by varying the printing pressure, bioink power-law coefficient, and the nozzle diameter can be controlled. The shear-thinning or -thickening of the bioink can be used to regulate deposition stability, create better cross-linking for gel formation and demonstrate the layer stacking process. In favor of this theoretical model, we have established a computational model using Fluent in chapter 3.

3.2 Theoretical Model

We considered an extrusion-based deposition of a viscous fluid thread leaving a nozzle and falling onto a stationary substrate (Figure 13). The nozzle, with diameter d and height H from the substrate, moves horizontally with a constant velocity V, and the fluid is released at the flow rate Q. We summarized the main considerations and assumptions underlying our model. We described a steady-state solution for the shape of the fluid jet from the nozzle to the substrate. The solution relies on the slenderness of the fluid jet and the absence of shear stresses on the free surface of the jet.

www.manaraa.com

Figure 13

Schematic representation of the bioink thread with a free-body diagram of a fluid element.

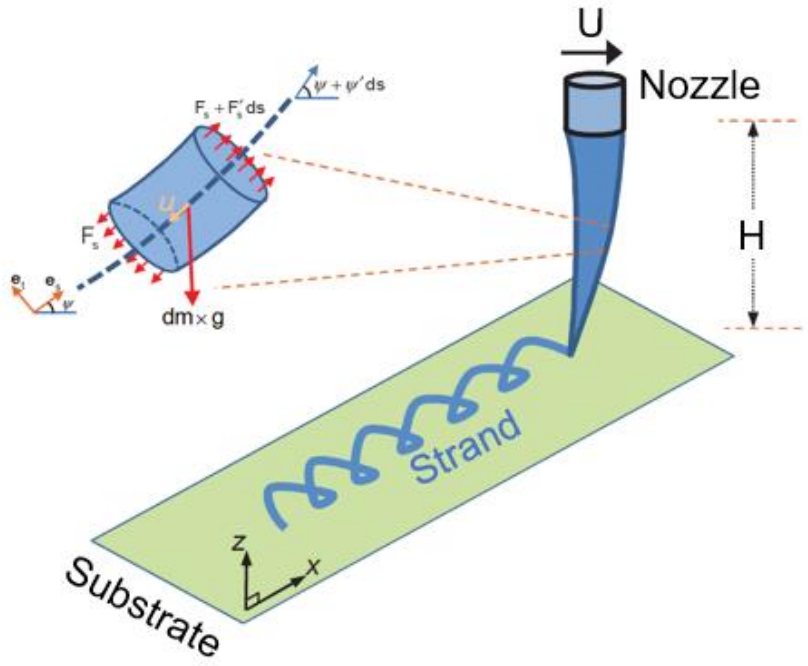

The nozzle is assumed to be a uniform cylindrical duct of a constant diameter, D, under pneumatic pressure. One can assume that the average shear rate within the bioink (assuming developed flow in the nozzle) is

$$Q = U_N \pi R_N^2 \qquad \text{(Eq.3.1)}$$

where R_N and $U_N$denote the radius of the nozzle tip and the average velocity of the bioink flow at the nozzle tip, respectively. The displacement field of the flow can be obtained from

www.manaraa.com

$D = \frac{1}{2}(L + L^T)$ Where L = ∇u is the gradient of the velocity vector u.

The axial and transverse equations of motion, after dropping the increment ds from both sides (see Figure 13), can be written as

$$\frac{dF_s}{ds} - \rho g A \sin\psi = \rho A a_s = \rho A U \frac{dU}{ds}, \qquad \text{(Eq.3.2)}$$

$$F_s \frac{d\psi}{ds} - \rho g A \cos\psi = \rho A a_t = \rho A U^2 \frac{d\psi}{ds}, \qquad \text{(Eq.3.3)}$$

with $F_s = A\sigma_{ss} + 2\pi R\gamma$ and $A = \pi^2$.

where the acceleration terms are derived from $Du_s/Dt = U\, d(Ue_s)/dt = UU'e_s + U\psi' e_t$

We assumed that the bioink behaves like a viscous fluid with a power-law stress-strain rate relationship. The total stress tensor for the bioink can be written in the form

$$\tau = K D_e^{(n-1)} D \qquad \text{(Eq.3.4)}$$

where K is the bioink consistency constant, *n* is the power-law index, and $D_e = \sqrt{2D \cdot D}$ is the equivalent strain-rate. The bioink exhibits a shear thickening and shear thinning behavior for *n* > 1 and *n* < 1, respectively. The special case of *n* = 1 corresponds to an Newtonian fluid, with K = μ being the dynamic viscosity of the fluid. The total stress can be written as

www.manaraa.com

$$\sigma = -pI + \tau \qquad \text{(Eq.3.5)}$$

Where p is the hydrostatic pressure in the fluid.

The boundary condition for the radial stress at the free surface r = R is given by $\sigma_{rr}|_{r=R} = \gamma / R$, which can be used to determine the hydrostatic pressure in Eq. (5). Substituting

p into (5), the axial force is obtained as

$$F_{ss} = -3AKD_e^{(n-1)}U' + \pi R\gamma \qquad \text{(Eq.3.6)}$$

$$T' = \frac{g\,sin\,\psi}{U}, \qquad T\psi' = \frac{g\,cos\,\psi}{U} \qquad \text{(Eq.3.7)}$$

$$T = -3D_e^{(n-1)}U' - U^2 + \frac{\gamma}{\rho}\sqrt{\pi U / Q} \qquad \text{(Eq.3.8)}$$

$$De = \sqrt{2\left[\left(\frac{\partial u_r}{\partial r}\right)^2 + \left(\frac{u_r}{r}\right)^2 + \left(\frac{\partial u_s}{\partial s}\right)^2\right]} \qquad \text{(Eq.3.9)}$$

$$De = \sqrt{3}|U'| \qquad \text{(Eq.3.10)}$$

Equations (3.7) can be combined and integrated to give.

$$T(s) = T_0\,sec\big(\psi(s)\big), \qquad \text{(Eq.3.11)}$$

www.manaraa.com

$$T_0 U\psi' = g\cos^2(\psi),$$

$$\left(\sqrt{3}\right)^{n+1}|U'|^{n-1}U' = -T_0\sec\left(\psi(s)\right) - U^2 + \frac{\gamma}{\rho}\sqrt{\pi U / Q} \qquad \text{(Eq.3.12)}$$

The above equations were solved with the initial and final boundary conditions

$$\psi(0) = 0°, \quad U(0) = U_0, \quad \psi|@Nozzle = \pi/2, \quad U|@Nozzle = Q/A \qquad \text{(Eq.3.13)}$$

$$x = \int_s \cos\left(\psi(s)\right),\ z = \int_s \cos\left(\psi(s)\right) \qquad \text{(Eq.3.14)}$$

The above equations can be written as

$$u_r = -(r/2)(\partial u_s/\partial s)$$

$$\sigma = \tau + (\gamma/r - p)I$$

$$p = KD_e^{(n-1)}\frac{dU}{ds} + \frac{\gamma}{R}$$

So far, we modeled the bioink as a homogeneous yield stress fluid deposition on a fixed substrate.

$$\tau = \widetilde{K}D_e^{(n-1)}D \qquad \text{(Eq.3.15)}$$

$$\widetilde{K} = (1-C)\left[\frac{\sqrt{2+3C}}{\sqrt{2}(1-C)}\right]^{n+1}K \qquad \text{(Eq.3.16)}$$

www.manaraa.com

3.3 Numerical Model Development

Supporting the work by Avaz et al., the numerical model was designed using the CFD software package ANSYS FLUENT 2020 R1. This two-dimensional, multi-phase model was developed to study the deposition of different viscous power-law fluids. All the fluids were assumed to be immiscible and incompressible. The Eulerian-Eulerian dependent Volume of Fluid (VOF) model was used since the two fluids share a relatively well-defined interface. Air is specified as the primary phase and power-law fluids as the secondary phase. The flow geometry is shown schematically in (Figure 14), and a representational image of the model is shown in (Figure 13). A nozzle of diameter (D) at the height of (H) from a moving substrate has been considered for the analysis. Various viscous non-Newtonian power-law fluids with a consistency index (k) and the power-law index (n) were flowed through the inlet individually. The density considered by all the power-law fluids is ρ. Fluid properties are shown in Table 1.

Figure 14

2D fluent model geometry representing boundaries and mesh details.

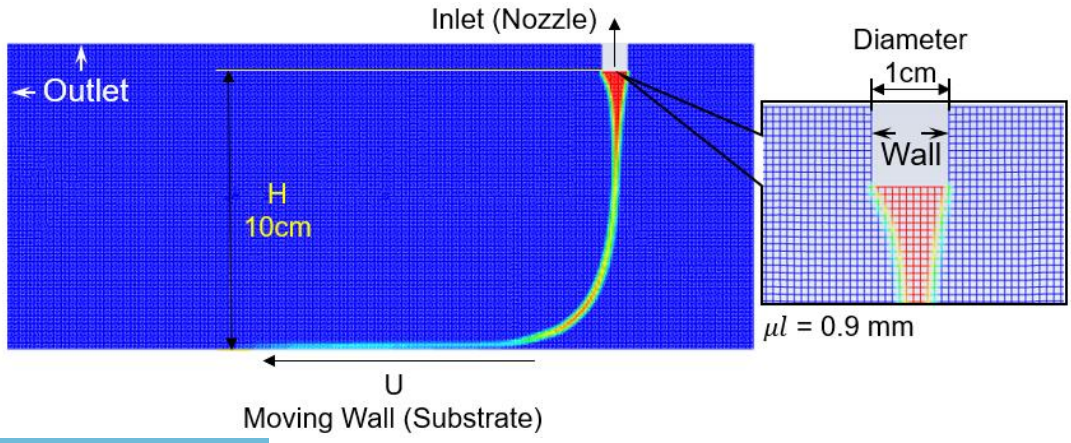

www.manaraa.com

Table 1

Material properties

Material	Density ρ (kg/m^3)	Dynamic viscosity	
		Consistency index k (Pa.s)	Power Law index n
Hydrogel	1126	499	0.7,0.9,1.0,1.1,1.5
Air	1.225	1.7894e-05	

A fine structured mesh was generated using adaptive sizing all through the geometry with control volume size (μl) as shown in (Figure 14) after performing grid analysis. The inlet and outlet boundary conditions were assumed to be velocity and pressure, respectively. For all the simulations, the inlet velocity is V cm/s, the equivalent to the volumetric flow rate Q cm^3/s, and the surface tension between the power-law fluid and the air is σ dyne/cm. A no-slip, no penetration boundary condition was imposed at the wall. The input parameters used for the model are listed in Table 2. The substrate is also a wall boundary, but with a translational speed of U cm/s, the nozzle position (Inlet) remained unchanged. However, since printhead and substrate movements are proportional and acceleration is expected to be zero, the model will cover the opposite scheme where the print head moves, and the substrate is constant. The domain was initialized with air and standard gravity g acting in a negative Y direction.

www.manaraa.com

Table 2

Parameters for the input model

Parameter	Nomenclature	Value	Units
D	Nozzle diameter	0.01	m
H	Height/gap distance of the nozzle	0.1	m
σ	Surface tension coefficient between air and hydrogels	60	mN/m
V	Substrate velocity	0.13	m/s
U	Fiber velocity from the inlet.	0.0056	m/s
g	Standard gravity acceleration	9.81	m/s^2

A schematic of the meshed geometry and the boundary conditions are shown in (Figure 14). A transient simulation with a time step μt = 0.25 sec was performed to capture the dynamic behavior of the fluid flow. Different methods were used for the discretization of the governing equations. A first-order upwind method was used to discretize the momentum equation since this scheme provides a proper representation of the fluid flow physics. For pressure-velocity coupling, Pressure Implicit with Splitting of Operators (PISO) is used.

3.4 Results

The first part of our results shows the fundamental behavior of non-Newtonian flow leaving the nozzle. Figure 15A(i) and 15A(ii) depicts the filament's shape between the nozzle and substrate for both theoretical and ANSYS Fluent model, respectively. The shear-thinning behavior of bioink yielded a smaller toe region while the increase in the

www.manaraa.com

power-law coefficient enlarged the toe region. This indicates the chance of being unstable during printing, where a raise of power-law coefficient from n=0.7 to n=1.5 yielded an eight-fold increase in the length of toe-region. Figure 15B(i) and 15B(ii) highlights the role of the same parameter in bioink velocity post-deposition.

Figure 15

A) Thread profile from nozzle to substrate (i) Theoretical (ii) Fluent B) Velocity post deposition (i)Theoretical (ii) Fluent.

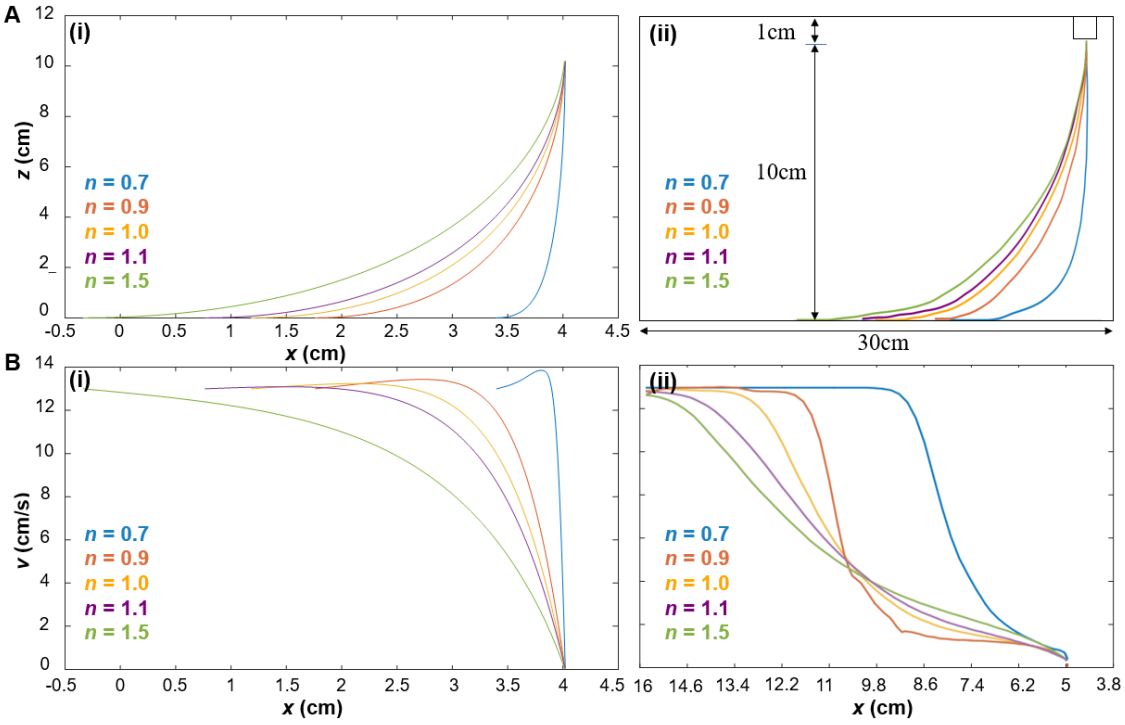

Using the fluent model, the variations of fiber shape after leaving the nozzle were depicted in (Figure 16A) for different power-law fluids and (Figure 16B) is representing the actual

www.manaraa.com

volume covered by bioink during deposition within each cell and the whole domain. The deposition of shear-thinning and -thickening fluids at different time steps showing the stable and unstable deposition are seen in (Figure 17).

Figure 16

A) Thread Profile B) Volume Fraction of the deposited bioinks.

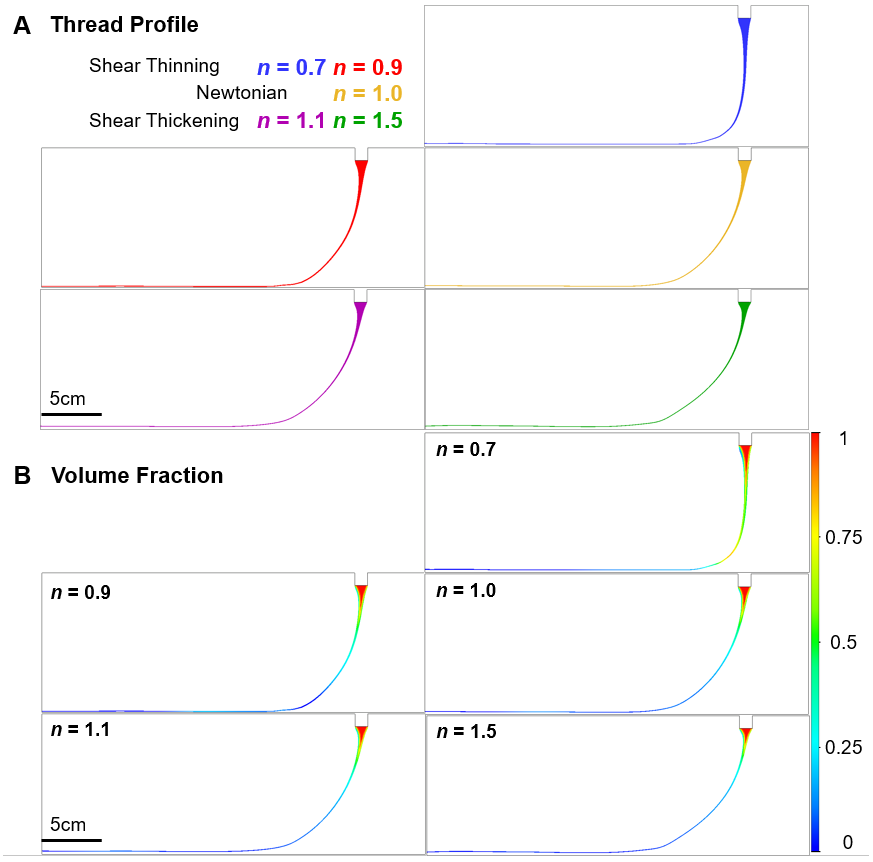

www.manaraa.com

Figure 17

Deposition of shear-thinning and -thickening bioinks at different time intervals.

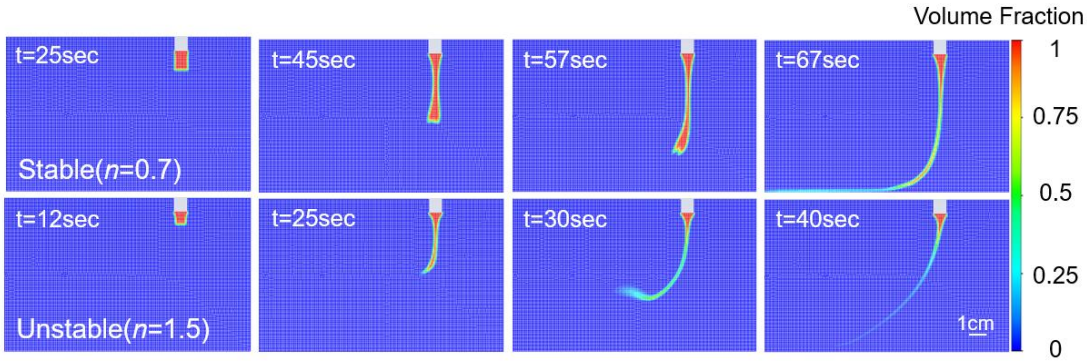

3.5 Discussion

In this chapter, we analytically studied the effects of shear-thinning on the physical behavior of bioink after leaving the nozzle. Shear thickening can be a consequence of cell concentrations, where the geometry of cells might regulate the power-law properties. In addition, hydrogel pore size and geometry on the behavior of the ink viscosity was analyzed. This shear thinning/thickening parameter may affect the deposition of bioinks. The theoretical model was based on Alginate, a widely used bioink model in biomedical engineering, mostly mixed with biological components for enhanced bioactivity. The presence of cells in the bioink influences the rheological properties, thus impacting the stability of extruded filament.

This work provides insight into the role of cellular components in the overall behavior of hydrogels when leaving printhead nozzle. This can be of importance for future works on modeling the behavior of cell-laden hydrogels. The region of stability is shifted

www.manaraa.com

by the presences of cells and this can be significant when considering the elasticity of cells (in this work, cells were assumed to be rigid particles).

Figure 18

The effect of shear thinning/thickening on the stability regions.

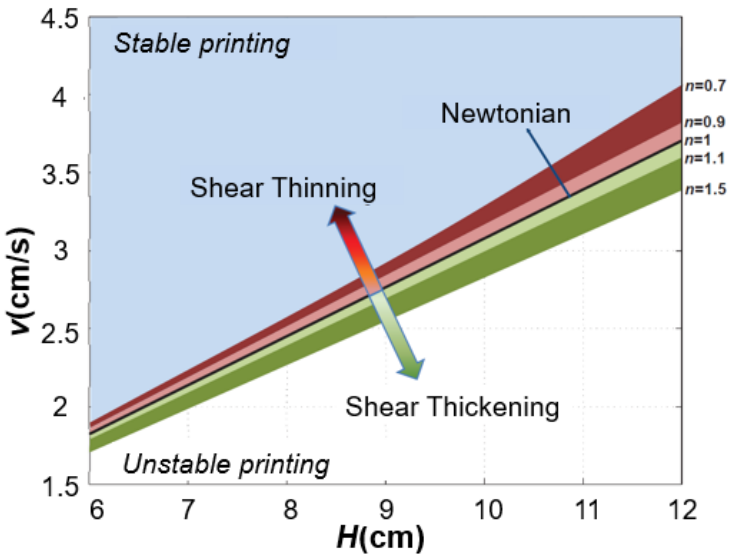

www.manaraa.com

Chapter 4

Numerical Simulation of Extrusion Bioprinting

4.1 Extrusion Bioprinting

The model aims to analyze the extrusion and the deposition of hydrogels in the region between the nozzle and substrate or previous layers. The distortion of the Fiber was simulated as a fluid flow within the paradigm of CFD. Fluid dynamics is governed by the law of conservation of mass and the conservation of linear momentum. To simplify our simulation, the following assumptions were made for the physics of fluid flow:

I. The material was considered incompressible with the constant density (ρ), and the mass conservation translates into volume conservation.

II. We assumed to be a creeping flow and the inertial effects are negligible compared to the viscous forces.

III. The hydrogel material was modeled with Non-Newtonian behavior, where the viscosity of the deposited fiber can be defined by a power-law index.

IV. The liquid adheres to the nozzle and the substrate and a no-slip condition was assigned to all the wall boundaries.

V. Extrusion-based bioprinting does not involve melting the filament material (temperature independent). The energy equation was turned off for all printing conditions, and the fiber deposition was considered isothermal.

As there are more than two immiscible fluids in the domain multi-phase VoF model was chosen to solve the momentum equation and trace the volume fraction for all the Eulerian phases. It includes two eulerian phases. The primary phase is the air, and various

www.manaraa.com

bioinks are the secondary phase. The fluent module does not have predefined materials for hydrogels; new fluids were created into the material library by specifying properties like density and dynamic viscosity. The density (ρ) and dynamic viscosity of distinct hydrogels are given in Table 3.

Table 3

Material properties of different phases used in the model

Material	Density ρ (kg/m^3)	Dynamic viscosity	
		Viscosity coefficient k (Pa.s)	Power-law index n
Bioink 1	1126	499	0.7
Bioink 2	1126	499	0.9
Air	1.225	1.7894e-05	

Figure 19

A) Geometry of the numerical model showing boundaries B) Details of the tetrahedral mesh.

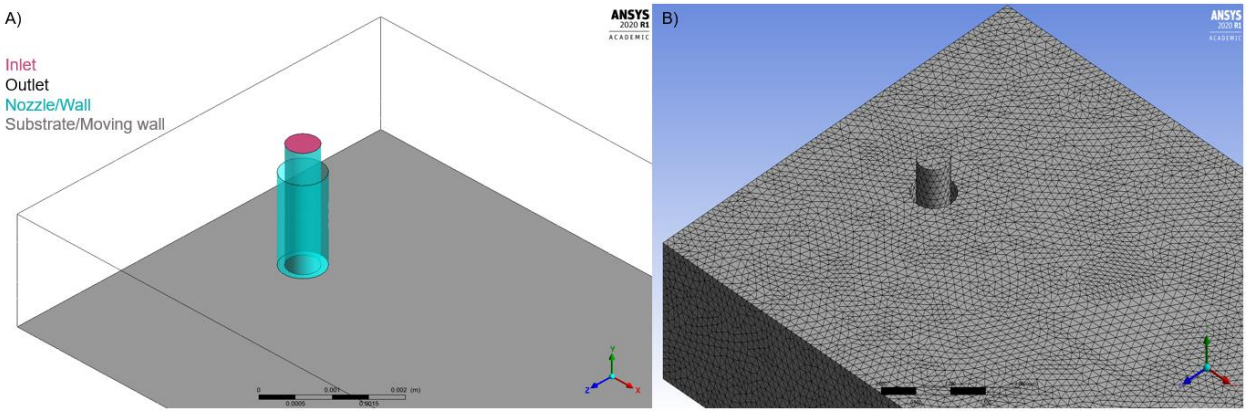

www.manaraa.com

4.1.1 Geometry and Mesh

The extruded fiber physics was studied by a computational model that involves the lower end of a standard extrusion nozzle and the distance between the printhead and substrate. In this model, the nozzle position was unchanged, while the substrate moves with a regulated speed. However, because the motions of the printhead and substrate are proportional to each other and the accelerations are assumed to be zero, the model can cover the opposite arrangement where the printhead shifts and the substrate is constant. Figure 19A represents the geometry of the numerical model. A cylindrical duct of inner diameter *D1* (0.5mm) and outer diameter *D2* (0.6mm) is the extrusion nozzle. The computational model assumes that the flow is laminar and completely developed at the nozzle exit. However, the length of the nozzle is unrelated to the discharge from the nozzle. The moving substrate was modeled by a perpendicular plane below the printhead, with a gap distance (*H)* from the nozzle exit. A rectangular domain occupies the outside of the printing nozzle. The numerical model's leftover exterior surfaces were outlet boundaries, where the substance is free to leave. The nozzle diameter *D* normalizes all the dimensions of the graphical model, while the velocity *V* of the traveling substrate normalizes the average velocity within the nozzle. Keeping the nozzle diameter and the substrate velocity constant (to avoid the effect velocity on the printed fiber), for various gap distances and multiple hydrogels, the fluid flow of the extruded fiber was simulated. Table 4 provides the numerical values chosen for the numerical simulations. Gravity was considered in the simulations in negative y-direction.

www.manaraa.com

Table 4

Parameters used in numerical simulation

Parameter	Nomenclature	value	units
D	Nozzle diameter	0.0005	m
H	Height/gap distance of the nozzle	(0.00025,0.00035)	m
σ	Surface tension coefficient between air and bioink	60	mN/m
V	Substrate velocity	0.0045	m/s
U	Fiber velocity from the inlet.	0.0045	m/s
G	Standard gravity acceleration	9.81	m/s^2

Fluid flow was simulated using the ANSYS Fluent R1 2020 program, based on the method of finite-volume. The Equations (2.24) and (2.25) are integrated over a finite set of volumes of tetrahedral regulation that meshes the domain of simulation. Tetrahedral mesh specifics are indicated in (Figure 19B). The rectangular domain was initialized with no traces of the bioink inside it; then, the fluid starts from the inlet traveling through the nozzle and depositing onto the moving substrate. A sample of the deposited fiber is shown in (Figure 20A).

The numerical solver computes discrete values of the continuous velocity and pressure fields at the center of the control volumes following a cell-centered discretization. Whenever required, the values at all other positions are interpolated from the discrete values. The numerical scheme evaluates across all the faces of the control volumes the advection and diffusion fluxes of momentum. Then according to the net fluxes, the cumulative amount of momentum within each control volume is modified. The pressure

www.manaraa.com

field is a function of the continuity restriction since the fluid is incompressible. The pressure equation is derived from the mass conservations.

Figure 20

A) Sample deposition of bioink B) Top and Side- view of extruded fiber for H = 0.25mm for H = 0.35mm C) Cut cross-section view of a printed fiber.

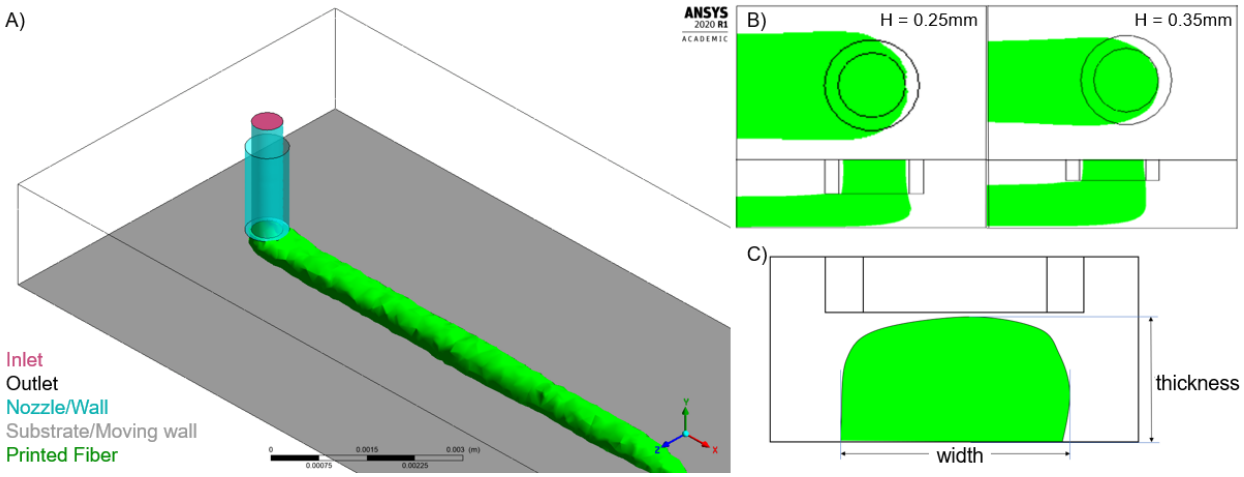

Also, an algebraic volume-of-fluid method which measures the transport of two additional field variables monitoring the location of the surface, captures the free surface of the extruded substance. For a study of the volume-of-fluid system, we refer readers to the following articles [44-47]. At normal time intervals, the progression of the system is solved incrementally. The accuracy of the numerical simulation depends on the time-step

www.manaraa.com

intervals and the size of the control volumes. The maximum size of the control volumes in our models is μl = 0.1 mm, and μt = 0.005 sec is the time-step interval. As the entire domain is wide and has few solver restrictions, the size of the control volume cannot possibly be reduced to improve precision. With an implicit solver that guarantees the consistency of the computational system, the discretized momentum equations and pressure equations corresponding to the set of control volumes were solved. The numerical algorithm computes the new values of the primary discrete variables at each incremental time step, which are the local velocities, the strain, and the location of the extruded fiber's free surface. Secondary outcomes were determined from the primary variables, such as the streamline of the flow, the wall shear stress, pressure exerted by the extruded fiber on the substrate, fiber velocity within the nozzle.

4.1.2 Morphology of the Printed Fiber

The shape of the printed Fiber was captured by the free surface-tracking algorithm. Figure 20B represents examples of top- and side-views of material deposition for two printing conditions: (a) small gap distance and (b) large gap distance. We see that the bioink spreads more on the substrate, at the front, and on the side of the printhead. For printing with a small gap, and the bioink has less side flow and prefers to stay at the back of the nozzle, for printing with a large gap. After the extrusion, the printed fiber quickly reaches a quiescent state. By virtue of the volume conservation, the volumetric flow rate of the material deposited on the moving substrate is the same as the volumetric flow rate in the nozzle. However, both the gap distance and velocity ratio influence the shape of the fiber cross-section. The velocities of the substrate and the fiber's velocity were kept constant throughout the simulated models. Then the crossection of the printed fiber for different gap

www.manaraa.com

distances were measured as shown in (Figure 20C) at different locations and and the average values are tabulated in Table 5. The thickness of the strand is often believed to be equal to the gap distance; however, our numerical results indicate that the thickness of the strand ranges between −5% and +5% of the gap size in the processing parameters that were investigated. As the fiber moves through the gap zone, the shear flow is rearranged into a uniform flow at velocity *V*, resulting in the shrinkage of the fiber due to the mass conservation of the material.

Table 5

Width and thickness of the fibers for different printing conditions

Nozzle Diameter 0.5mm	Width		Thickness	
	Power Law Index (0.7)	Power Law Index (0.9)	Power Law Index (0.7)	Power Law Index (0.9)
H = 0.35 mm	0.6 mm	0.68 mm	0.35 mm	0.33 mm
H = 0.25 mm	0.8 mm	0.89 mm	0.25 mm	0.24 mm

4.1.3 Printing Pressure

To overcome the flow resistance coming from the fluid's adherence to the nozzle wall, the viscous flow creates a pressure gradient around the extrusion nozzle. The Hagen-Poiseuille Law describes the pressure gradient P_z driving the laminar creeping flow within the nozzle:

$$P_z = \frac{32\mu U}{D^2} \qquad \text{(Eq.4.1)}$$

www.manaraa.com

A printing force *F* is applied to the substrate by the extruded material, which refers to the pressure field integral minus a *Patm* gauge pressure over the substrate's surface.

$$F = \int_{Substrate} (P - P_{atm})\, dS \qquad \text{(Eq.4.2)}$$

The average viscous stress τ_a inside the nozzle is standardized by the value of the pressure field

$$\bar{P} = (P - P_{atm})/\tau_a \qquad \text{(Eq.4.3)}$$

Where,

$$\tau_a = \mu\dot{\gamma}_a \qquad \text{(Eq.4.4)}$$

μ is the dynamic viscosity of the fluid and $\dot{\gamma}_a$ is the average shear-rate of the fully-developed laminar pipe flow.

The normalized pressure distribution on the substrate is represented for different heights of the nozzle and different non-newtonian fluids. As expected, the extruded material applies a larger pressure on the substrate when the gap distance is small. For the printing conditions with a small gap (Figure 21A) H = 0.25 mm, the extruded material applies a pressure field almost axisymmetric, with the maximum pressure just below the nozzle's center. For larger gaps (Figure 21B) H = 0.35mm, the pressure level drops and is slighty concentrated towards the front end of the nozzle, Also, the fiber with power-law

www.manaraa.com

n=0.7 the pressure exerted comparatively low compared to the pressure exerted by the fiber with power-law n= 0.9.

Figure 21

Pressure exerted on the moving substrate for A) H = 0.25 mm B) H = 0.35 mm for power law index 0.7 and 0.9.

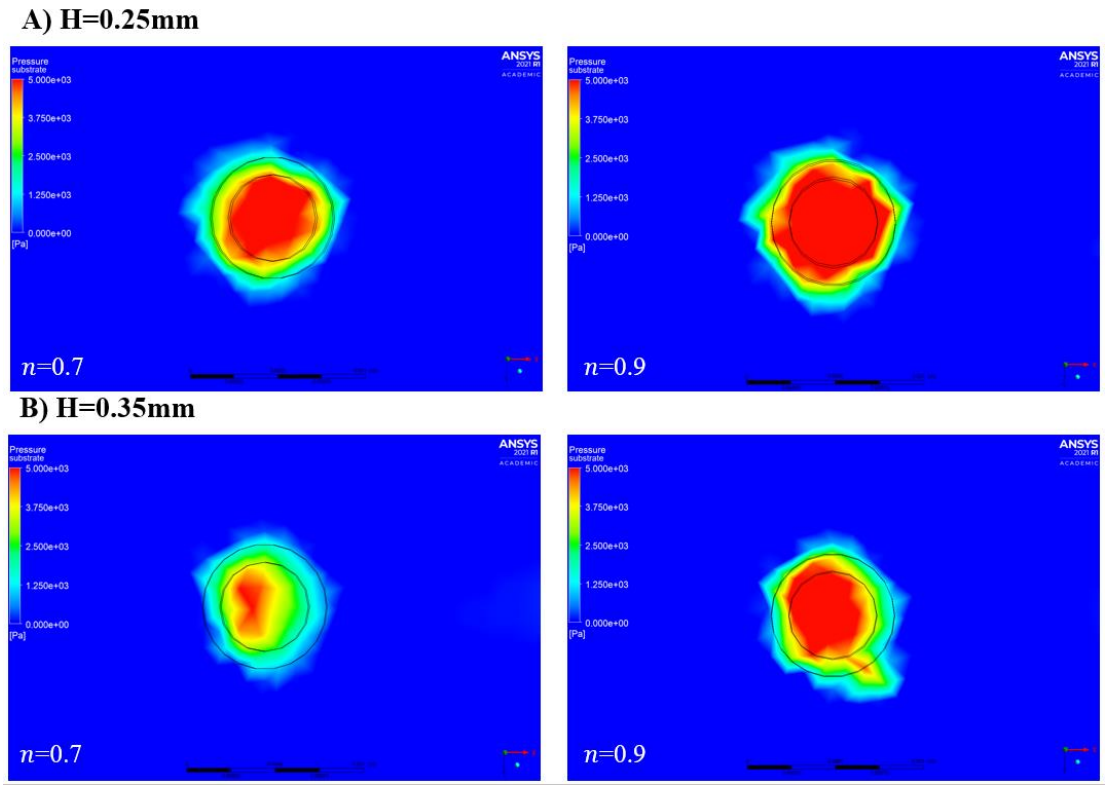

4.1.4 Wall Shear Stress

The tangential force per unit area exerted on the surface of the duct tube by the moving fluid is known as wall shear stress (WSS). The magnitude of WSS is proportional

www.manaraa.com

to the gradient of velocity near the wall of the tube, i.e., how quickly the velocity of flow changes as it travels from a point on the wall of the tube to an exactly opposite point in a normal direction (i.e., perpendicular) to the wall of the tube towards the middle of the tube. Low WSS values are correlated with low local speeds and, hence, long fluid residence times in the near-wall area. This gradient of velocity near the wall is called the wall shear rate. The WSS value τ_w is defined as proportional to the wall shear rate.

$$\tau_w = \mu \dot{\gamma}_w \qquad \text{(Eq.4.4)}$$

where μ is the dynamic viscosity of the fluid and $\dot{\gamma}_w$ is the wall shear stress

The shear stress on the moving substrate is shown for different heights of the nozzle and different non-newtonian fluids. The fiber depositing on the substrate when the gap distance is small generates more shear forces as more of the fluid is passing in the gap distance. For the printing conditions with a small gap (Figure 22A) H = 0.25 mm, the shear stress on the moving wall is almost axisymmetric, with the maximum stress toward the front end of the nozzle and fades away in the direction of the substrate movement. For larger gaps (Figure 22B) H = 0.35 mm, the shear stress drops and is concentrated towards the center of the nozzle. For fiber with the value of n = 0.7, the shear stress on the moving substrate is comparatively low, with the fiber's stress with n = 0.9.

www.manaraa.com

Figure 22

Wall shear generated on moving substrate for A) H = 0.25 mm B) H = 0.35 mm for power law index 0.7 and 0.9.

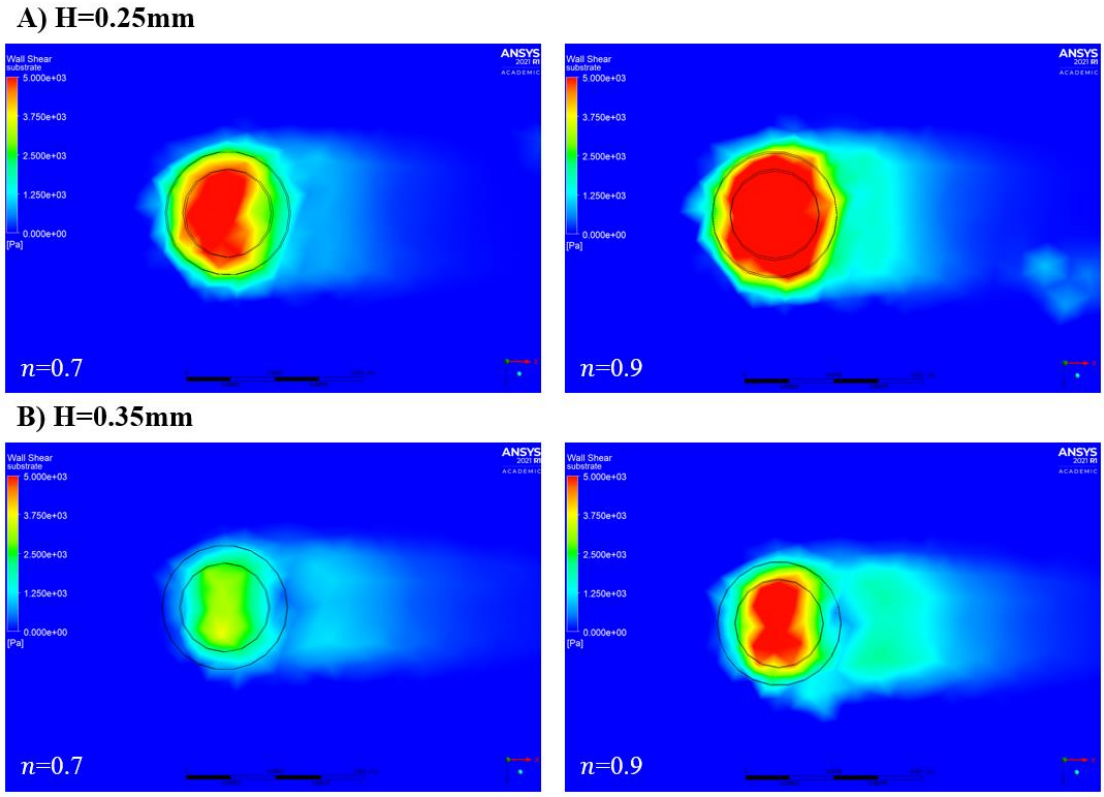

The velocity of the fiber inside the nozzle from the inlet to the moving substrate, is plotted for different power-law fluids and for different gap distances H = 0.25 mm and H = 0.35 mm in (Figure 23) and (Figure 24), respectively As the fiber begins with the initial velocity U (0.0045 m/s) and approaches the substrate velocity V (0.0045 m/s) after deposition, the plotting takes place within this range along the path from the inlet to the substrate.

www.manaraa.com

Figure 23

Plots representing the fiber velocity from nozzle to substrate at nozzle height H = 0.25 mm.

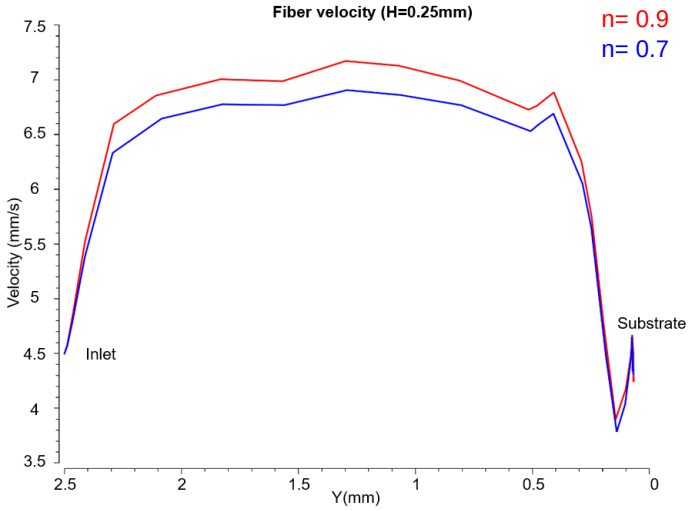

Figure 24

Plots representing the fiber velocity from nozzle to substrate at nozzle height H = 0.35 mm.

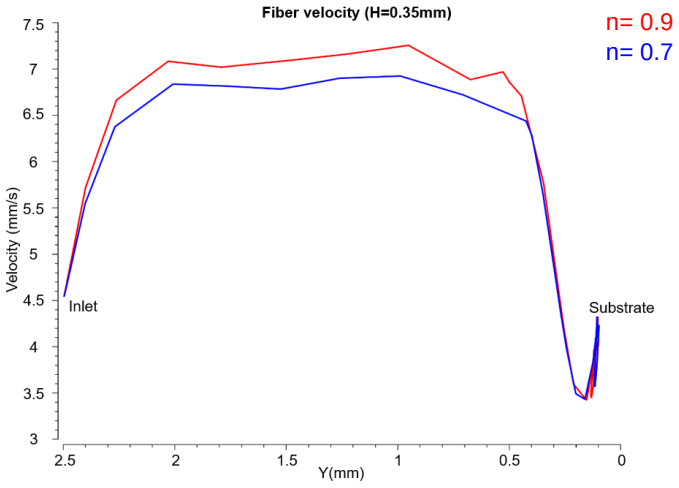

www.manaraa.com

4.2 Coaxial Bioprinting

The model shown below of a coaxial nozzel demonstrates the different flow behavior of the hydrogels. The geometry is the same as above, except that two fluids were flown simultaneously through the nozzle, as shown in (Figure 25A).

Figure 25

A) Geometry of the coaxial nozzle B) Details of tetrahedral mesh C) Cut cross-sectional view of coaxial extruded fiber to measure dimensions.

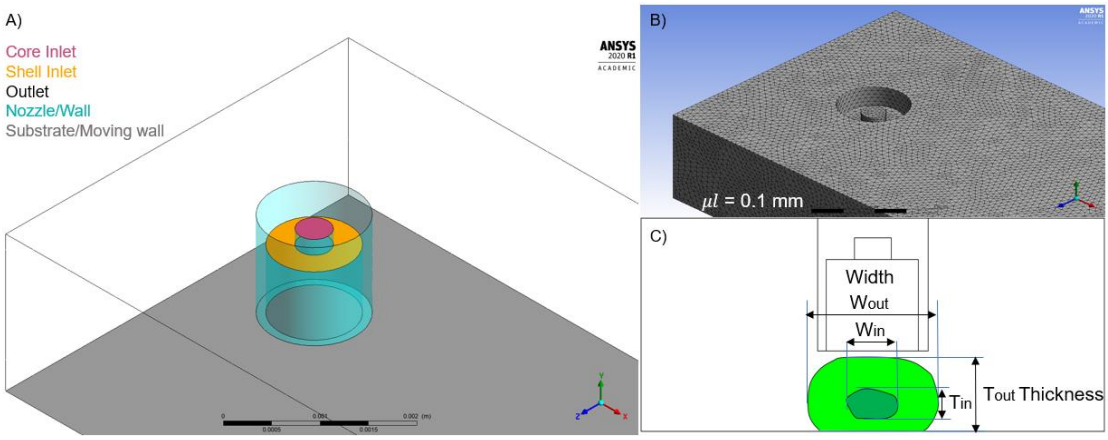

The specifications of the Tetrahedral mesh are seen in (Figure 25B) with the control volumes and the time- step interval as earlier with μl = 0.1 mm, and μt = 0.005 sec, respectively. Figure 25C shows how the physical dimensions are taken for the extruded fibers. The fibers were extruded for two different heights (H = 0.5 mm and H = 0.75 mm). The overall diameter of a coaxial nozzle was compared to a single nozzle and the heights were increased in coaxial printing to make the fiber flow easy. The same bioinks from

www.manaraa.com

(Table 3) were used here, but they flowed through different nozzles for each height. For better understanding, the thread exiting the shell nozzle was made transparent and specific colors have been assigned to each hydrogel. The hydrogel with a power-law index of 0.7 is colored blue, and the hydrogel with a power-law index of 0.9 is colored red for all the coaxial 3D bioprinting processes. The updated parameters are listed in Table 6.

Table 6

Parameters used for coaxial model

Parameter	Nomenclature	value	units
Dc	Core nozzle diameter	0.0005	m
Ds	Shell nozzle diameter	0.001	m
H	Height/gap distance of the nozzle	(0.0005,0.00075)	m
σ	Surface tension coefficient between air and hydrogels	60	mN/m
V	Substrate velocity	0.0045	m/s
U	Fiber velocity from the nozzle	0.0045	m/s
g	Standard gravity acceleration	9.81	m/s^2

4.2.1 Results for Nozzle Height H=0.5mm

The core nozzle is a diameter of 0.5 mm, and the shell nozzle is 1 mm diameter. For the nozzle height of H = 0.5 mm, the results were drawn and presented first for each hydrogel streaming from separate nozzles. For the corresponding cut cross-section views (Figure 26) and (Figure 29), the average physical dimensions are tabulated in Table 7 and Table 8 respectively. For each printing state, 3D figures of the isosurface are viewed in

www.manaraa.com

(Figure 27) and (Figure 30). Below the isosurface estimates, the contours of the pressure gradient and the wall shear stress are shown in (Figure 28) and (Figure 31).

Table 7

Physical dimensions of the printed fiber for Figure 26

Nozzle Diameter	Width	Thickness
Core Nozzle (0.5 mm)	0.62 mm	0.21 mm
Shell Nozzle (1 mm)	1.75 mm	0.5 mm

Figure 26

Cut cross-section view of the printed strand from Figure 27.

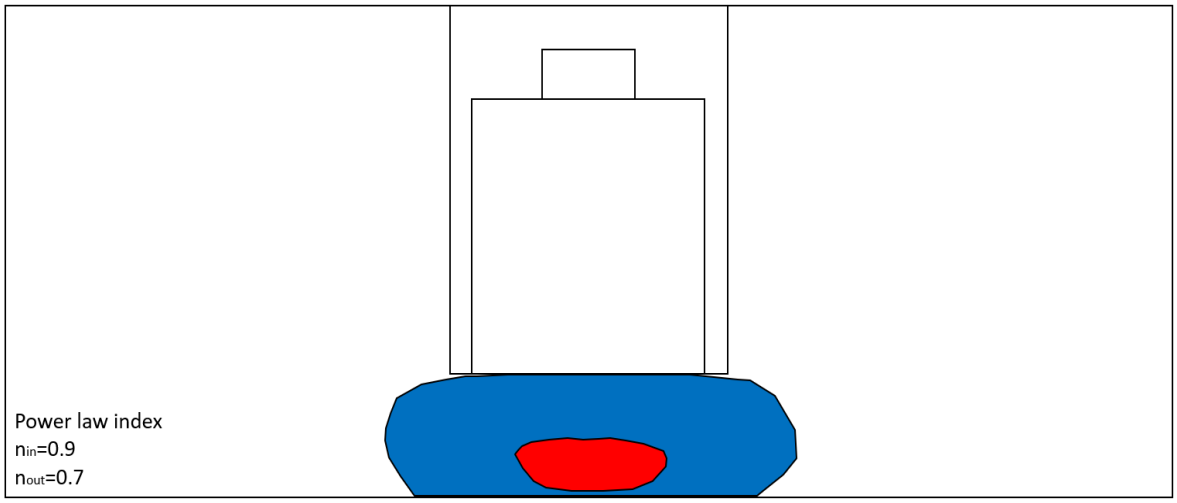

www.manaraa.com

Figure 27

Isosurface of the printed fiber where bioink with the power-law index of 0.7 as the shell and bioink with the power-law index of 0.9 as the core.

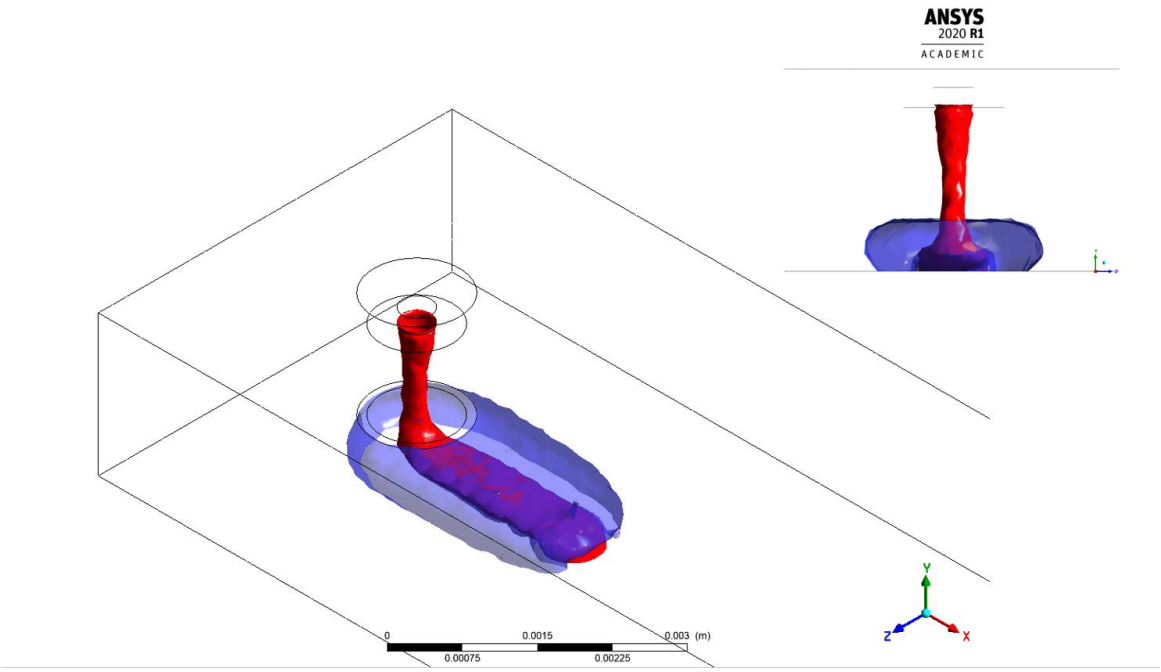

Figure 28

Contours of pressure gradient and wall shear on the moving substrate for Figure 27.

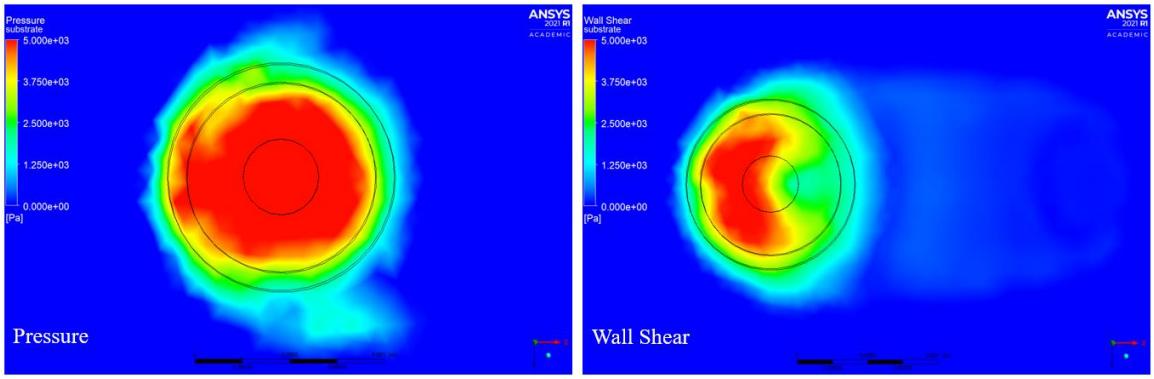

www.manaraa.com

Table 8

Physical dimensions of the printed fiber for Figure 29

Nozzle Diameter	Width	Thickness
Core Nozzle (0.5 mm)	0.67 mm	0.16 mm
Shell Nozzle (1 mm)	1.80 mm	0.50 mm

Figure 29

Cut cross-section view of the printed strand from Figure 30.

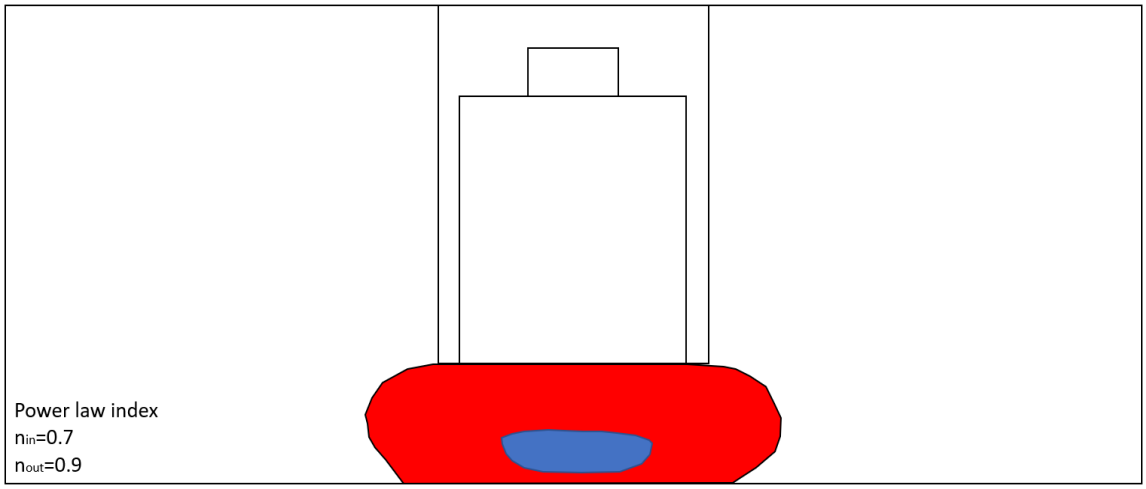

www.manaraa.com

Figure 30

Isosurface of the printed fiber where bioink with the power-law index of 0.9 as the shell and bioink with the power-law index of 0.7 as the core.

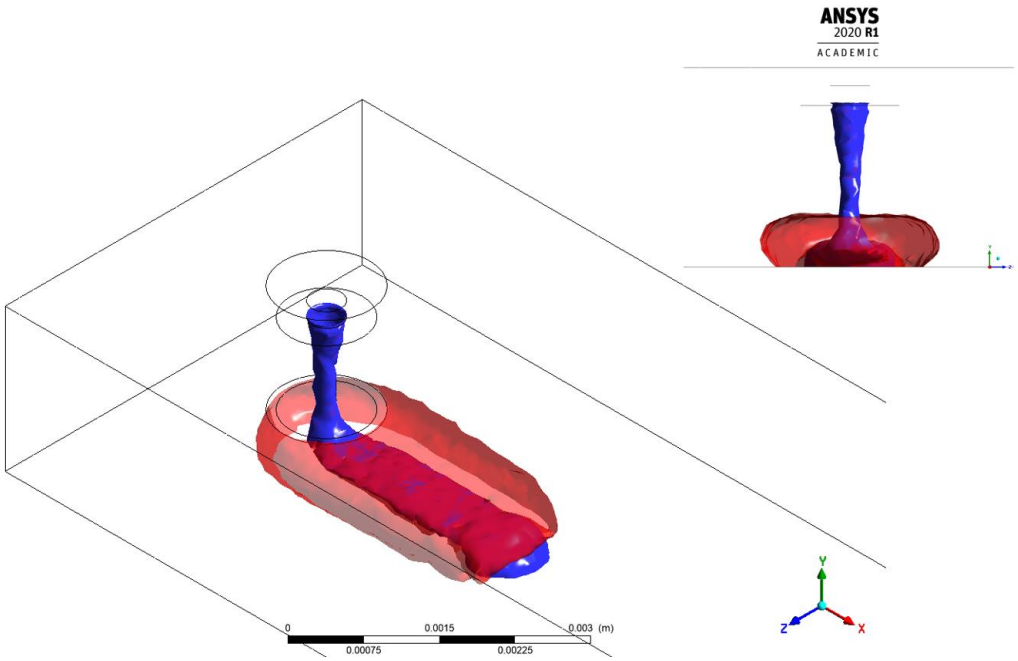

Figure 31

Contours of pressure gradient and wall shear on the moving substrate for Figure 30.

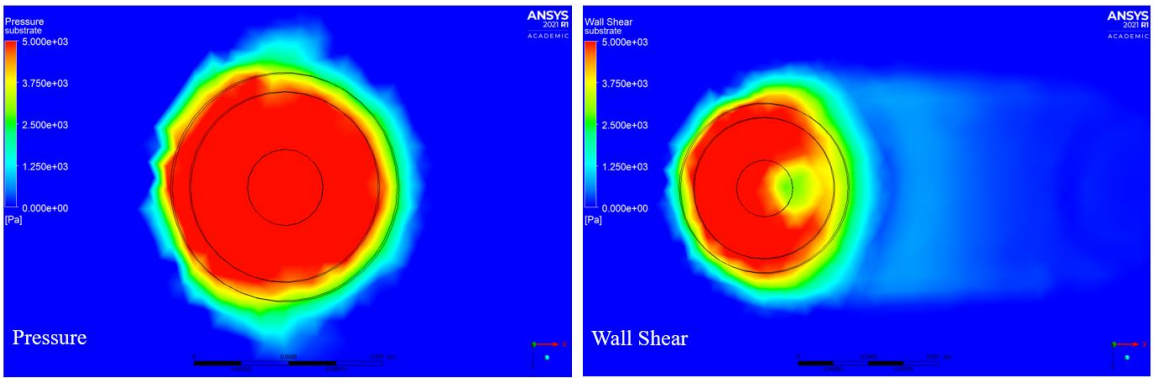

www.manaraa.com

For the nozzle height H = 0.5 mm, each hydrogel's velocity for the core and shell plotted within the nozzle in Figure 32.

Figure 32

Plots representing the fibers velocity from nozzle to substrate coaxially at nozzle height H = 0.5 mm.

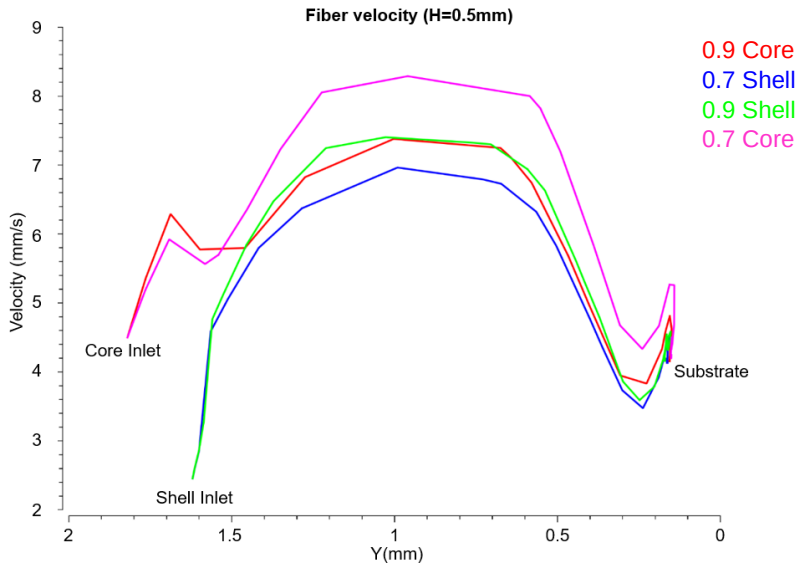

4.2.2 Results for Nozzle Height H = 0.75 mm

As the nozzle height H=0.5mm is low the fiber deposted looks compressed and is out of shape. The nozzel diameters remained the same and the nozzle height was increased to H = 0.75 mm. The deposition was recorded in the results and presented first for each

www.manaraa.com

hydrogel streaming from separate nozzles. The corresponding cut cross-section views (Figure 33) and (Figure 36), the physical dimensions are tabulated in Table 9 and Table 10, respectively. For each printing state, 3D figures of the isosurface are viewed in (Figure 34) and (Figure 37). Then, the pressure gradient and the wall shear stress contours are shown in (Figure 35) and (Figure 38) below them.

Table 9

Physical dimensions of the printed fiber for Figure 33

Nozzle Diameter	Width	Thickness
Core Diameter (0.5 mm)	0.50 mm	0.26 mm
Shell Diameter (1 mm)	1.37 mm	0.74 mm

Figure 33

Cut cross-section view of the printed strand from Figure 34.

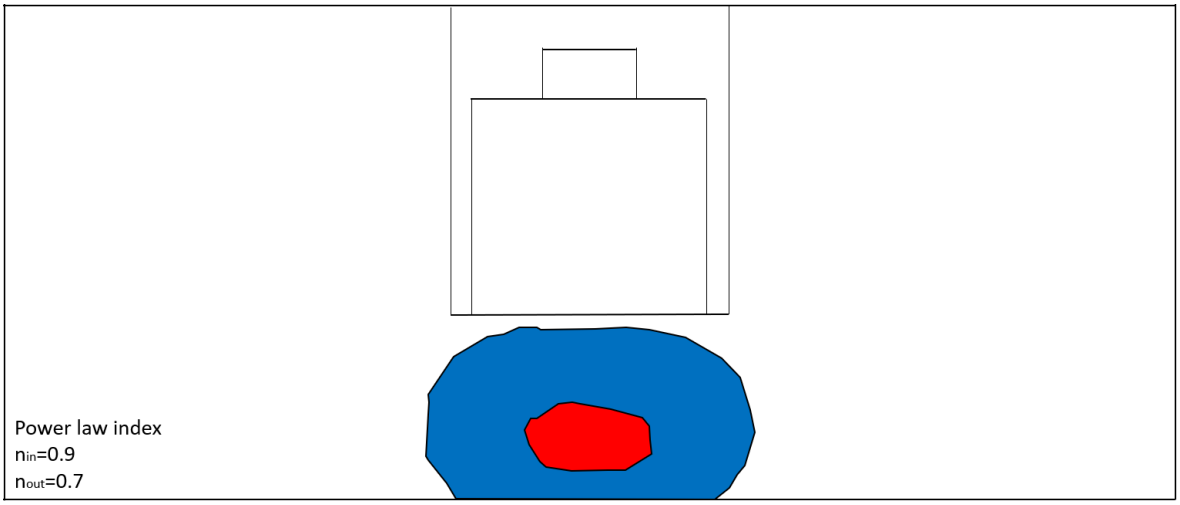

www.manaraa.com

Figure 34

Isosurface of the multi-layer fiber where bioinks with the power-law index of 0.7 as the shell and 0.9 as the core.

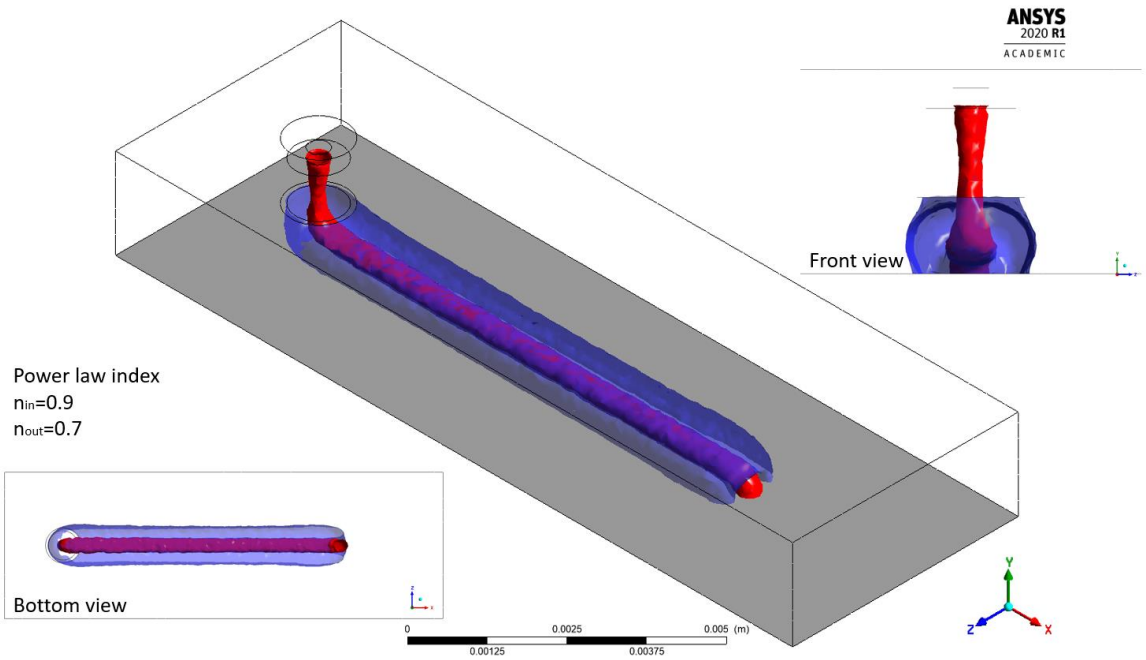

Figure 35

Contours of pressure gradient and wall shear on the moving substrate for Figure 34.

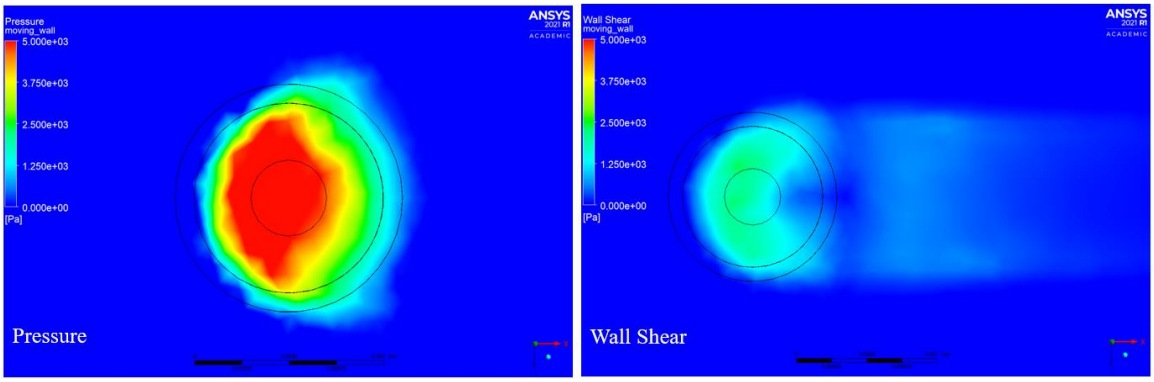

www.manaraa.com

Table 10

Physical dimensions of the printed fiber for Figure 36

Nozzle Diameter	Width	Thickness
Inner Diameter (0.5 mm)	0.56 mm	0.24 mm
Outer Diameter (1 mm)	1.51 mm	0.73 mm

Figure 36

Cut cross-section view of the printed strand from Figure 37.

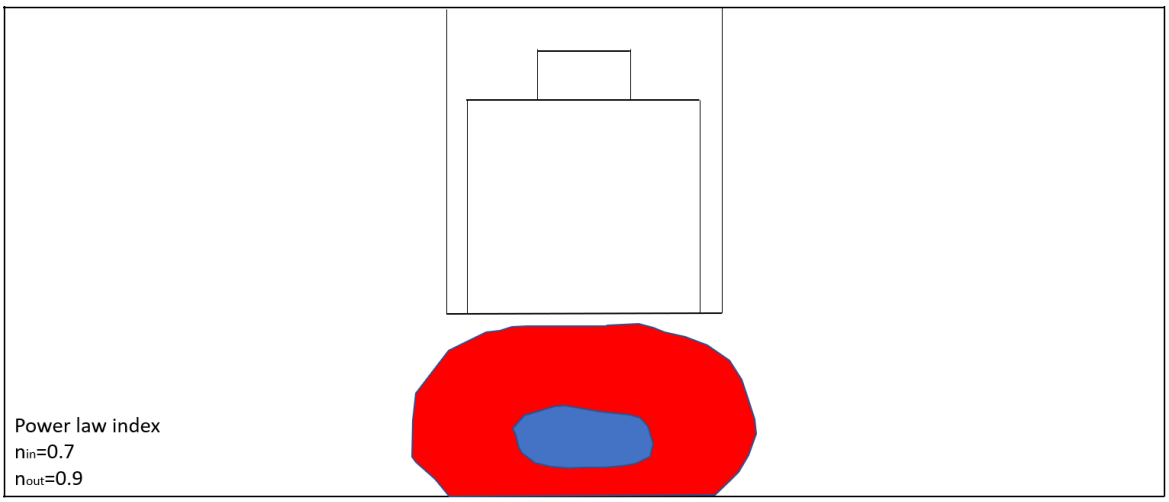

www.manaraa.com

Figure 37

Isosurface of the multi-layer fiber where bioinks with the power-law index of 0.9 as the shell and 0.7 as the core.

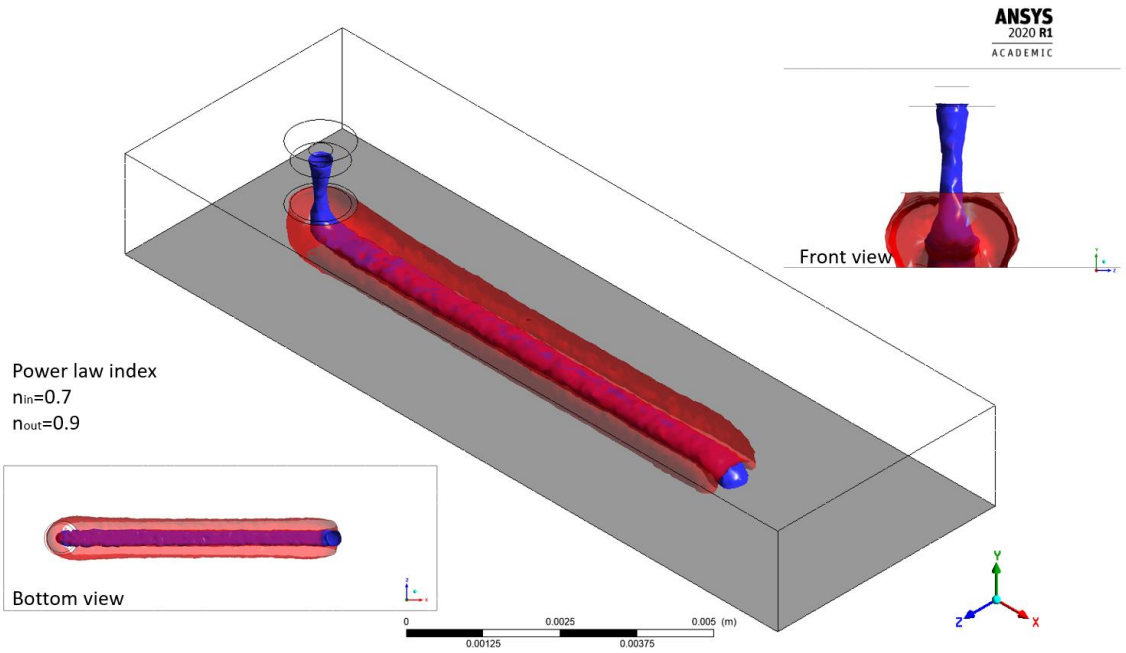

Figure 38

Contours of pressure gradient and wall shear on the moving substrate for Figure 37.

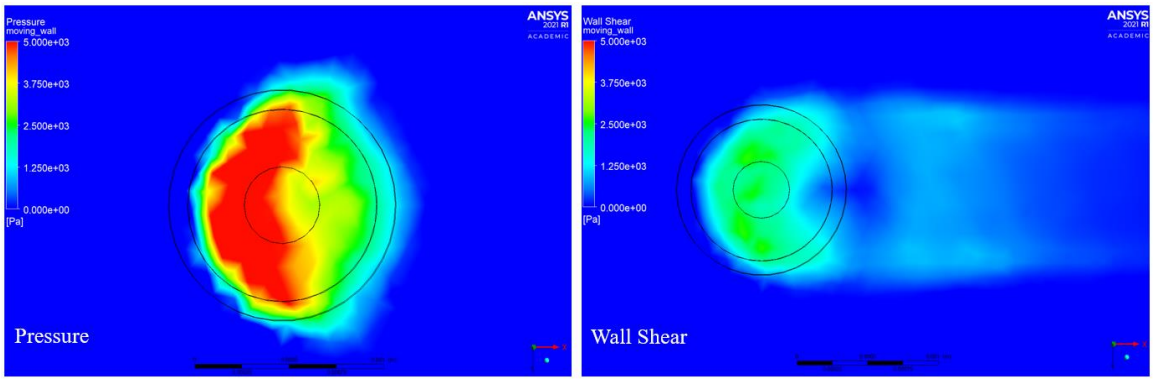

www.manaraa.com

Figure 39

Plots representing the fibers velocity from nozzle to substrate coaxially at nozzle height H = 0.75 mm.

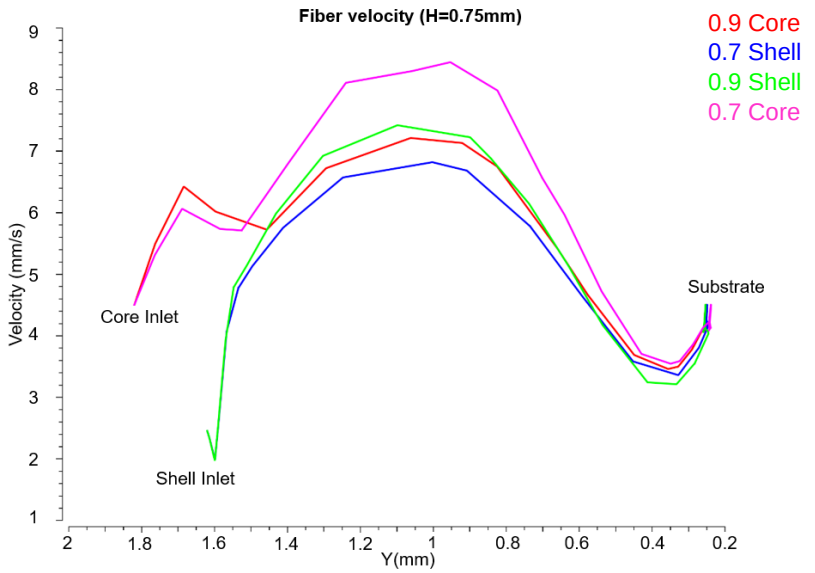

4.2.3 Mixing of Bioinks

The whole fiber was separated into the core and the shell and then using volume fraction (shows the space occupied by a fluid phase inside a cell or the whole domain) contour for both core and shell ink. In the top two contours, dark orange shows more concentration of the regional ink and light blue shows less concentration. The combined fiber below was divided into 5 regions depending on the mixing proportion of each bioink over the other. For Region I the volume of the core ink is more than 80%, region II is covered by 60 to 80% of the core ink and 20 to 40 % of the shell ink, region III has an equal proportion of both core and the sell inks, region IV show 20 to 40 % of the volume

www.manaraa.com

is the core ink and 60 to 80% of the volume is the shell ink and region V shows more than 80% of the volume is covered with the shell ink. (Figure 40) for the bioinks with power-law of 0.7 as shell and 0.9 as core. (Figure 41) for the bioinks with power-law of 0.7 as core and 0.9 as shell.

Figure 40

Mixing of bioink where fluid with the power-law index of 0.7 as the shell and fluid with the power-law index of 0.9 as the core.

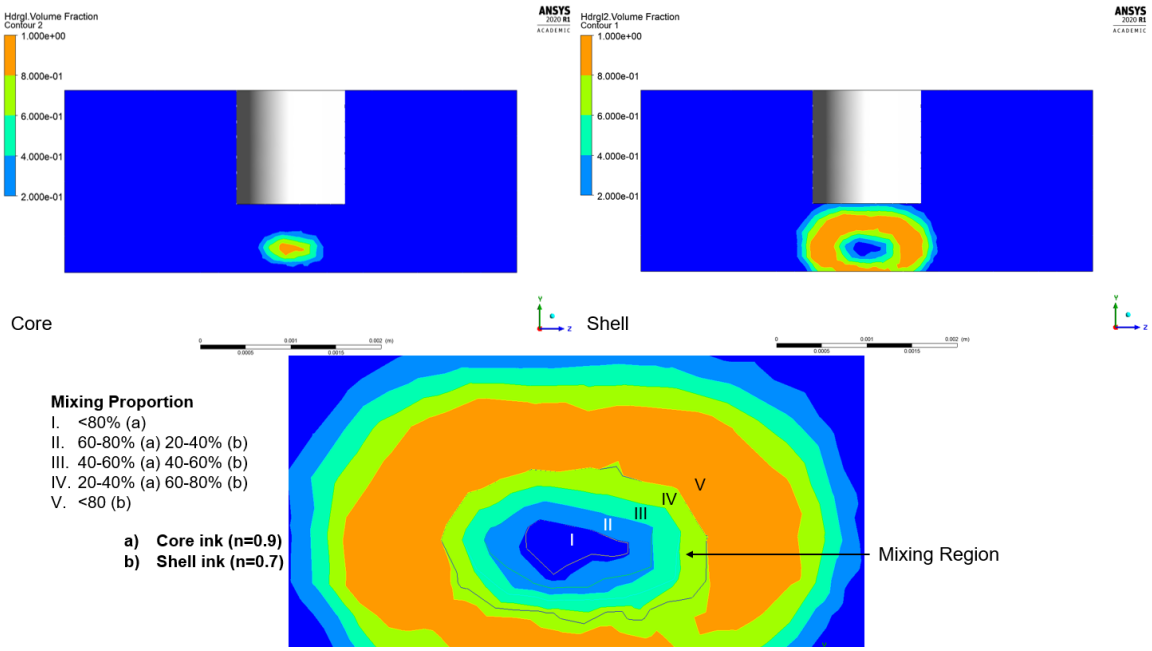

www.manaraa.com

Figure 41

Mixing of bioink where fluid with the power-law index of 0.9 as the shell and fluid with the power-law index of 0.7 as the core.

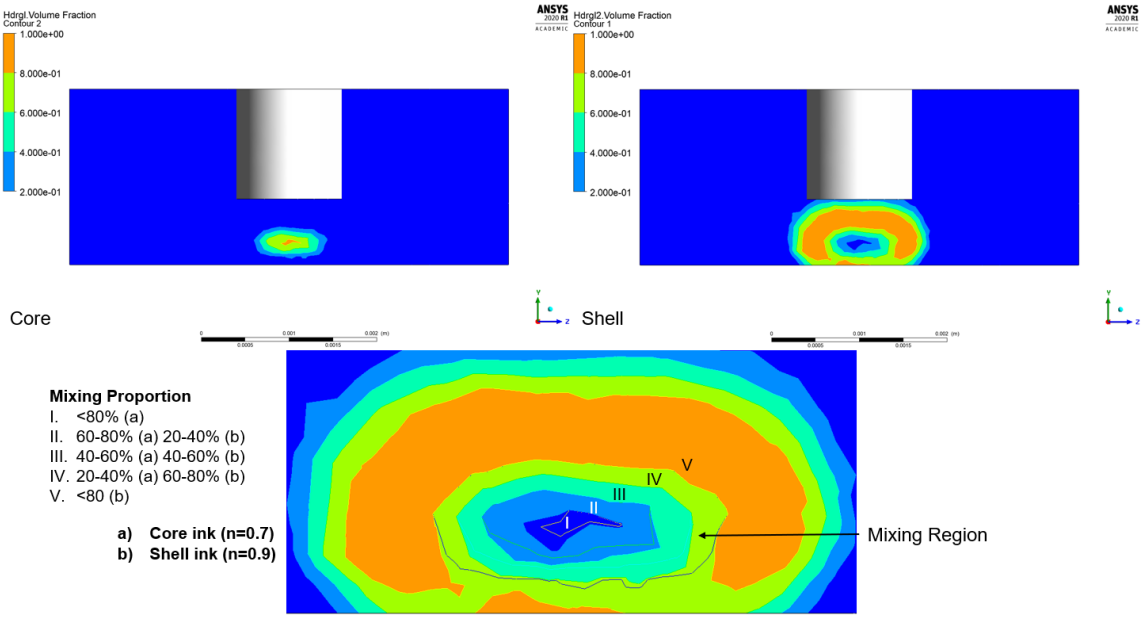

www.manaraa.com

Chapter 5

Diffusion

5.1 Introduction

Recent 3D bioprinting practices enable the creation of micro-tissues by utilizing cell-laden bioinks while safeguarding the basic orientation of the desired tissue. 3D printing techniques have been utilized to craft the supportive frame and microfluidic encasement in Organ-on-a-Chip (OoC) platforms[78]. One significant victory benchmark in the production of OoC platforms is the structural reliability of the bioprinted micro-tissues, determined by the minimum feature size known as the bioprinting resolution. OoC platforms intend to imitate the functions of tissues and organs, linking the difference between the traditional models based on planar cell cultures/animals and the complex human structure. These structures aim to recapitulate the complications found in vivo, using developments in microfluidic technologies and 3D cell culture techniques, [79] which includes: 3D structure; heterogeneous cellularity; cell-cell interactions; the presence of a complex extracellular matrix (ECM); perfused vasculature; and biomechanical forces (e.g., fluid flow-generated shear forces).

In recent years, attempts to build micro physio-logical systems (MPS) have focused on recreating human organs at the level of their smallest functional unit for toxicity testing and selective drug screening, such as the heart, liver, lung, and brain. Also, multiple "disease-on-a-chip" platforms have been built for basic science research to model human diseases. While these organ-on-a-chip platforms have shown substantial advances over conventional 2D monolayer culture systems in mimicking human organs and disease

www.manaraa.com

stages, in many cases, they are still at the proof-of-concept level. Many of these platforms require the operation and maintenance of specific peripheral equipment and facilities, and therefore may not be best equipped for larger-scale compound screening. A simple microfluidic device is designed to mimic the diffusion process of blood vessels, which supply the nutrients, and a scaffold (gel) where nutrients can diffuse while housing the cells. The factors which are needed to study the diffusiveness of these supplies are the porosity of the system, the velocities of the fluids flow inside the channels, the size of the channels, and the pressure distribution around the device.

5.2 Background Equations

Darcy's Law: to describe the flow through a porous medium.

$$q = \frac{-k}{\mu}\nabla p \qquad \text{(Eq.5.1)}$$

Where q is instantaneous flow rate, k is permeability, μ is dynamic viscosity of fluid, and ∇p is the pressure drop.

Navier-Stokes equation for a porous model

$$\frac{\partial(\rho U)}{\partial t} + \nabla \cdot (\rho UU) = -\nabla_p + \nabla \cdot \left(\mu\left((\nabla U) + (\nabla U)^T\right)\right) - \frac{2}{3}\mu(\nabla \cdot U)I + \rho g + S \qquad \text{(Eq.5.2)}$$

www.manaraa.com

A source term S is added to the Navier-Stokes equation to account the porous zone in each control volume. The x component of the source term is given by

$$S_x = -\left(\frac{C_1}{t}U_x + \frac{C_2}{t}\frac{1}{2}\rho|U|U_x\right) \quad \text{(Eq.5.3)}$$

$\frac{C_1}{t} = \frac{\mu}{\alpha}$; α is Viscous resistance/Absolute inverse permeability, $\frac{C_2}{t}$ is Inertial resistance.

5.3 Diffusion Model

The four solids containing a rectangular block act as the porous zone 1 (Figure 42C), was planted with three cylinders, two of them acting like channels. Another circular block in the center acts as porous zone 2 (Figure 42D). To study the flow inside the channels, they were considered solids. The channels were placed across the rectangular block's width, and the circular block was placed at the center of the rectangular block.

Figure 42

A) Geometry showing boundary conditions B) Tetrahedral mesh details C,D) Porous zone locations.

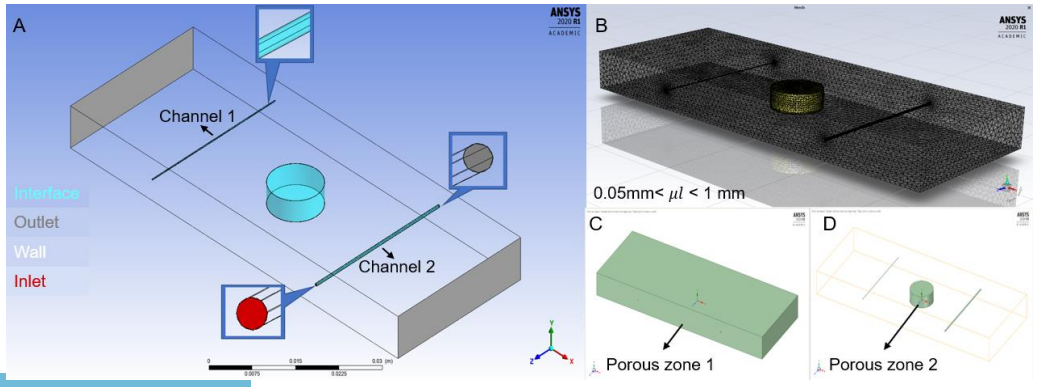

www.manaraa.com

Dimensions: Rectangular Block: Length = 80mm, Width = 30mm, Thickness = 8mm. Channel 1: Diameter = 0.25m, length = 30mm. Channel 2: Diameter = 0.5mm, length = 30mm. Circular Block: Diameter = 10mm, Thickness = 4mm.

Water flows with a velocity of 2m/s from both inlets of the channels. The interface between the channel and rectangular block acts as an outlet for the channel and as an inlet to the porous zone. The rectangular block and the cylindrical block are two different porous zones. The interface acts as an outlet for the rectangular block and an inlet for the circular block. Water can exit through the outlets and is constrained by the walls, as shown in (Figure 42A). The water that enters the channel starts to diffuse through the porous media. The porous zone conditions shown in Table 11 are considered to represent various hydrogels or fine sand. The flow throughout the zones is considered laminar.

Table 11

Porous zone conditions

Zone	Viscous Resistance ($1/m^2$) (x, y, z)	Inertial Resistance (1/m) (x, y, z)	Porosity (0 to 1)
Zone 1 (Rectangular Block)	1.2e+10	350000	0.9
Zone 2 (Circular Block)	1.2e+09	35000	0.9

A VOF multi-phase model was considered, with the primary phase as air and the second phase as water. The whole process was simulated as isothermal and under gravity

www.manaraa.com

in a negative y-direction. As the channels were considerably small compared to the rectangular block, meshing is done very fine (element size = 0.05 and 0.1). The whole geometry was meshed using tetrahedral elements with a maximum element size of 1mm, as shown in (Figure 42B).

5.4 Results

The results were studied as transient with step size μt = 0.1 sec for 50 sec. The pressure contour and the volume fraction of water were extracted every 12.5 sec. The diffusion inside the porous zone 1 is shown by the shaded region, which is colored with the pressure gradient in (Figure 43) and inside the porous zone 2 in (Figure 44). At 50 sec the pressure is plotted inside the channels in (Figure 45).

Figure 43

Pressure contour in porous zone 1.

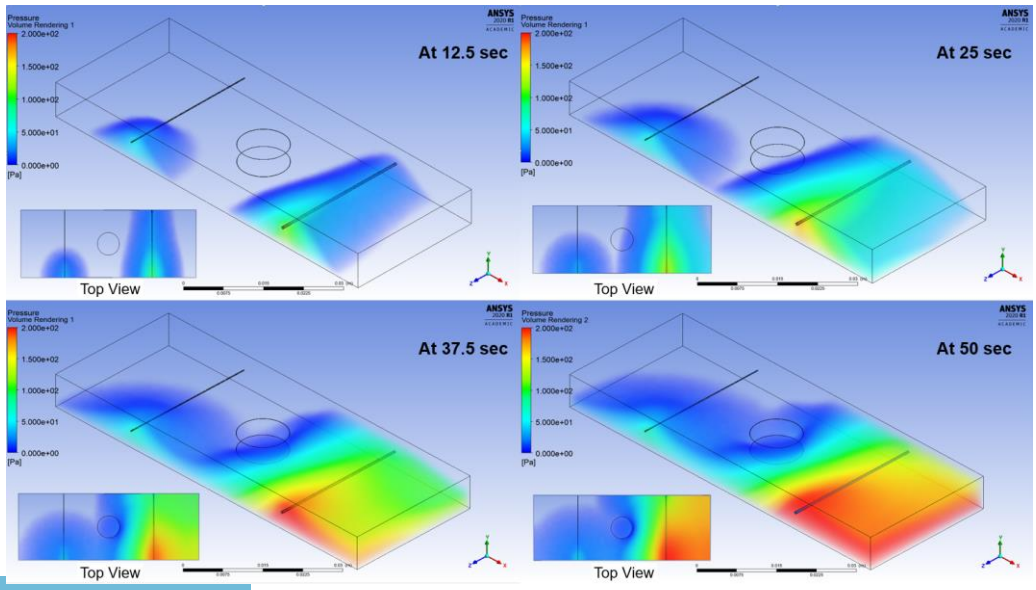

www.manaraa.com

Figure 44

Pressure contour in porous zone 2.

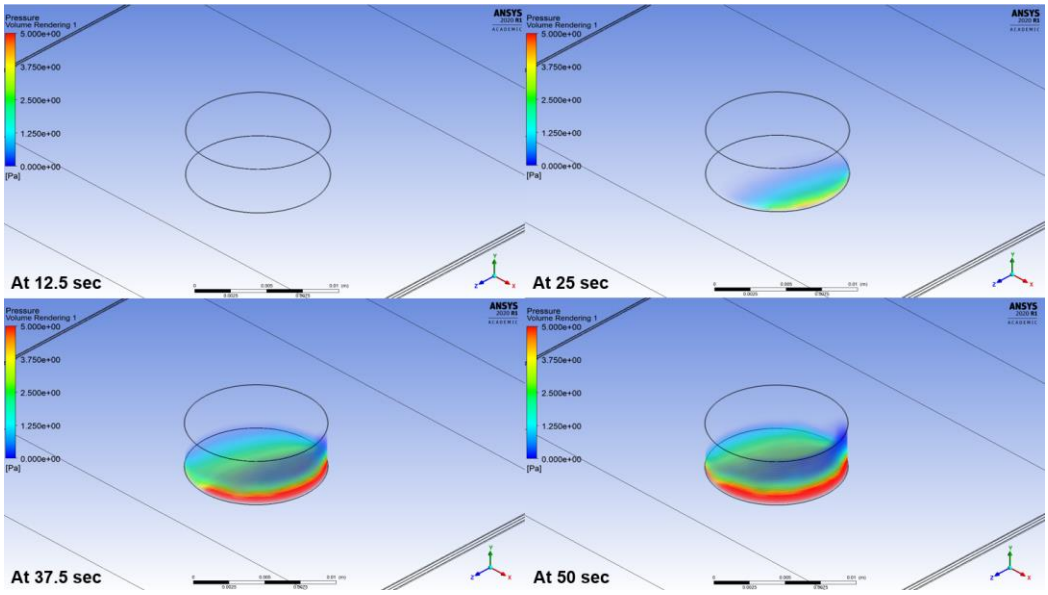

Figure 45

Pressure plot inside the channels.

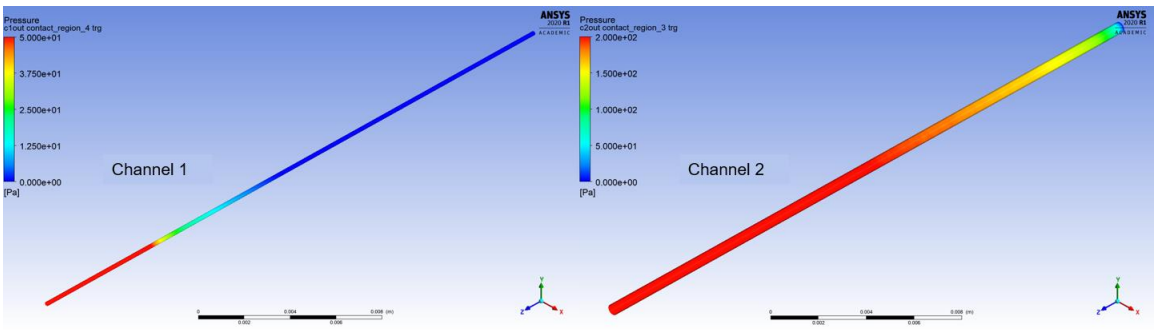

www.manaraa.com

Chapter 6

Conclusion and Future Scope

6.1 Conclusion

The numerical model is developed as additional data for the theoretical work by Avaz et al., (Bioink Instability in Extrusion Bioprinting: Role of Shear Thinning). During deposition, the fiber profile and fiber velocity of various bioinks in numerical modeling showed a similar trend with theoretical work. Additional data like volume fraction and fiber deposition at different time steps can also be calculated using numerical analysis. The shear-thinning/-thickening parameter influences the stability of printing. Both the theoretical and numerical approaches show that shear-thinning fluids provide more stable printing than that of shear-thickening fluids.

A CFD model is developed to simulate the process of 3D bioprinting. For this model two stable shear-thinning fluids were considered. These fluids were deposited using both single and coaxial nozzle heads. The parameters such as shape of the printed fiber, printing pressure, fiber velocity and wall shear stress in the system can be studied using CFD model. A uniform moving speed of the nozzle in single fiber deposition height of the nozzle has shown variations in all of the above parameters for both of the power-law fluids. In coaxial bioprinting, as both fluids are deposited at the same time the morphology of the multi-layer fiber, mixing of two fluids can also be examined. Like the single axial bioprinting the nozzle height and the position of the bioink flow (Core/Shell) influences mixing proportion, shape of the multi-layer fiber, printing pressure, relative flow velocities of the bioink and the wall shear stress inside the system. The fibers deposited through single

www.manaraa.com

and coaxial nozzles with larger heights has retained a good shape and had low printing pressure compared to smaller nozzle heights.

One of the applications of bioprinting which is solute diffusion in a hydrogel system can also be modelled using this software. An example model showing the fluid diffusion from a microfluidic channel into a hydrogel system was developed. Using this diffusion model, the pressure gradient inside the system for different porous zones were observed at different time intervals. For the same flow velocities in different sized channels the pressure plots inside each channel were extracted.

6.2 Future Scope

A lot of new concepts have been raised through this study that may lead to continued research. Firstly, as the models shown in this project are basic predictions made to simulate actual scientific problems experimental validation is needed. There are few other items for the future of this initiative that can be concentrated on. One of the major printability parameters is the printing speed, which is kept constant in the above bioprinting models. The changes in the shape of the fiber, printing pressure, etc. can be studied for various printing speeds.

Modelling multiple fibers next to each other can lead a whole new area of research for predicting the full-fledged bioprinted construct, interaction of two fluid fibers next to each other, porosity, and stiffness of the structure, etc. This can help us build a bioprinted microfluidic device where drug permeability, perfusion testing, etc., can be explored through numerical modeling.

www.manaraa.com

References

[1] J. A. Lewis and G. M. Gratson, "Direct writing in three dimensions," *Mater. today*, vol. 7, no. 7–8, pp. 32–39, 2004.

[2] S. Didari, Z. Y. Ahmad, J. D. Veldhorst, and T. A. L. Harris, "Wetting behavior of the shear thinning power law fluids," *J. Coatings Technol. Res.*, vol. 11, no. 1, pp. 95–102, 2014.

[3] E. Lepowsky, M. Muradoglu, and S. Tasoglu, "Towards preserving post-printing cell viability and improving the resolution: Past, present, and future of 3D bioprinting theory," *Bioprinting*, vol. 11, p. e00034, 2018.

[4] L. Ning and X. Chen, "A brief review of extrusion-based tissue scaffold bio-printing," *Biotechnol. J.*, vol. 12, no. 8, p. 1600671, 2017.

[5] X. B. Chen, and Schoenau G, and W. J. Zhang, "On the flow rate dynamics in time-pressure dispensing processes," *J. Dyn. Sys., Meas., Control*, vol. 124, no. 4, pp. 693–698, 2002.

[6] H. Valkenaers, F. Vogeler, A. Voet, and J.-P. Kruth, "Screw extrusion based 3D printing, a novel additive manufacturing technology," 2013.

[7] "Abdominal Key," 2018, [Online]. Available: https://abdominalkey.com/3d-bioprinting-for-tissue-engineering/.

[8] X. B. Chen, "Modeling of rotary screw fluid dispensing processes," 2007.

[9] L. Bian, C. Hou, E. Tous, R. Rai, R. L. Mauck, and J. A. Burdick, "The influence of hyaluronic acid hydrogel crosslinking density and macromolecular diffusivity on human MSC chondrogenesis and hypertrophy," *Biomaterials*, vol. 34, no. 2, pp. 413–421, 2013.

[10] C. J. Little, N. K. Bawolin, and X. Chen, "Mechanical properties of natural cartilage and tissue-engineered constructs," *Tissue Eng. Part B Rev.*, vol. 17, no. 4, pp. 213–227, 2011.

[11] Y. Nishiyama *et al.*, "Development of a three-dimensional bioprinter: construction of cell supporting structures using hydrogel and state-of-the-art inkjet technology," *J. Biomech. Eng.*, vol. 131, no. 3, 2009.

[12] I. Levental, P. C. Georges, and P. A. Janmey, "Soft biological materials and their impact on cell function," *Soft Matter*, vol. 3, no. 3, pp. 299–306, 2007.

[13] W. Liu *et al.*, "Coaxial extrusion bioprinting of 3D microfibrous constructs with cell-favorable gelatin methacryloyl microenvironments," *Biofabrication*, vol. 10, no. 2, p. 24102, 2018.

[14] "Magipics." https://www.youtube.com/channel/UC3jWNWu3F5iG4YdZCrWc1Fw.

www.manaraa.com

[15] M. H. Kim and S. Y. Nam, “Assessment of coaxial printability for extrusion-based bioprinting of alginate-based tubular constructs,” *Bioprinting*, vol. 20, p. e00092, 2020.

[16] Q. Gao, Y. He, J. Fu, A. Liu, and L. Ma, “Coaxial nozzle-assisted 3D bioprinting with built-in microchannels for nutrients delivery,” *Biomaterials*, vol. 61, pp. 203–215, 2015.

[17] J. Gopinathan and I. Noh, “Recent trends in bioinks for 3D printing,” *Biomater. Res.*, vol. 22, no. 1, p. 11, 2018.

[18] M. Hospodiuk, M. Dey, D. Sosnoski, and I. T. Ozbolat, “The bioink: a comprehensive review on bioprintable materials,” *Biotechnol. Adv.*, vol. 35, no. 2, pp. 217–239, 2017.

[19] A. Panwar and L. P. Tan, “Current status of bioinks for micro-extrusion-based 3D bioprinting,” *Molecules*, vol. 21, no. 6, p. 685, 2016.

[20] M. Guvendiren, H. D. Lu, and J. A. Burdick, “Shear-thinning hydrogels for biomedical applications,” *Soft Matter*, vol. 8, no. 2, pp. 260–272, 2012.

[21] R. Nair and A. R. Choudhury, “Synthesis and rheological characterization of a novel shear thinning levan gellan hydrogel,” *Int. J. Biol. Macromol.*, 2020.

[22] J. D. Anderson, “Computational Fluid Dynamics. The basics with applications. McGraw-Hill Science/Engineering/Math,” 1995.

[23] “Andrew Baker.” https://sites.google.com/site/ee535test/andrew-baker.

[24] M. A. Yardimci, S. I. Guceri, M. Agarwala, and S. C. Danforth, “Part quality prediction tools for fused deposition processing,” 1996.

[25] C. McIlroy and P. D. Olmsted, “Disentanglement effects on welding behaviour of polymer melts during the fused-filament-fabrication method for additive manufacturing,” *Polymer (Guildf).*, vol. 123, pp. 376–391, 2017.

[26] S. F. Costa, F. M. Duarte, and J. A. Covas, “Thermal conditions affecting heat transfer in FDM/FFE: a contribution towards the numerical modelling of the process: This paper investigates convection, conduction and radiation phenomena in the filament deposition process,” *Virtual Phys. Prototyp.*, vol. 10, no. 1, pp. 35–46, 2015.

[27] D. K. Ahn, J. H. Kweon, J. H. Choi, and S. H. Lee, “Relation between surface roughness and overlap interval in fused deposition modeling,” in *Advanced Materials Research*, 2011, vol. 264, pp. 1625–1630.

[28] A. Bellini, “Fused deposition of ceramics: a comprehensive experimental, analytical and computational study of material behavior, fabrication process and equipment design.” Drexel University Philadelphia, PA, 2002.

www.manaraa.com

[29] N. Mostafa, H. M. Syed, S. Igor, and G. Andrew, “A study of melt flow analysis of an ABS-Iron composite in fused deposition modelling process,” *Tsinghua Sci. Technol.*, vol. 14, pp. 29–37, 2009.

[30] B. P. Heller, D. E. Smith, and D. A. Jack, “Effects of extrudate swell and nozzle geometry on fiber orientation in Fused Filament Fabrication nozzle flow,” *Addit. Manuf.*, vol. 12, pp. 252–264, 2016.

[31] C. McIlroy and P. D. Olmsted, “Deformation of an amorphous polymer during the fused-filament-fabrication method for additive manufacturing,” *J. Rheol. (N. Y. N. Y).*, vol. 61, no. 2, pp. 379–397, 2017.

[32] R. B. Comminal, J. H. Hattel, and J. Spangenberg, “Numerical simulations of planar extrusion and fused filament fabrication of non-Newtonian fluids,” *Nord. Rheol. Soc. Annu. Trans.*, vol. 25, pp. 263–270, 2017.

[33] H. Xia, J. Lu, S. Dabiri, and G. Tryggvason, “Fully resolved numerical simulations of fused deposition modeling. Part I: fluid flow,” *Rapid Prototyp. J.*, 2018.

[34] J. Du, Z. Wei, X. Wang, J. Wang, and Z. Chen, “An improved fused deposition modeling process for forming large-size thin-walled parts,” *J. Mater. Process. Technol.*, vol. 234, pp. 332–341, 2016.

[35] X. Fang *et al.*, “Study on metal deposit in the fused-coating based additive manufacturing,” *Procedia Cirp*, vol. 55, pp. 115–121, 2016.

[36] M. E. Mackay, Z. R. Swain, C. R. Banbury, D. D. Phan, and D. A. Edwards, “The performance of the hot end in a plasticating 3D printer,” *J. Rheol. (N. Y. N. Y).*, vol. 61, no. 2, pp. 229–236, 2017.

[37] K. Y. Jiang and Y. H. Gu, “Controlling parameters for polymer melting and extrusion in FDM,” in *Key Engineering Materials*, 2004, vol. 259, pp. 667–671.

[38] A. Bellini, S. uk Gu¨ c¸ eri, and M. Bertoldi, “Liquefier dynamics in fused deposition,” *J. Manuf. Sci. Eng.*, vol. 126, no. 2, pp. 237–246, 2004.

[39] S. Bukkapatnam and B. Clark, “Dynamic modeling and monitoring of contour crafting—An extrusion-based layered manufacturing process,” 2007.

[40] Y. Tlegenov, Y. San Wong, and G. S. Hong, “A dynamic model for nozzle clog monitoring in fused deposition modelling,” *Rapid Prototyp. J.*, 2017.

[41] A. K. Miri *et al.*, “Effective bioprinting resolution in tissue model fabrication,” *Lab Chip*, vol. 19, no. 11, 2019.

[42] R. Comminal, M. P. Serdeczny, D. B. Pedersen, and J. Spangenberg, “Numerical modeling of the strand deposition flow in extrusion-based additive manufacturing. Addit Manuf 20: 68–76.” 2018.

www.manaraa.com

[43] Marcin P.SerdecznyRaphaëlComminalDavid B.PedersenJonSpangenberg, "Experimental validation of a numerical model for the strand shape in material extrusion additive manufacturing," [Online]. Available: https://www.sciencedirect.com/science/article/pii/S2214860418304585?casa_token=cvbSdJdgG8EAAAAA:nLgs2wA4FmSf-0em2fHExWZVNH28YhXfmJX8ty94qhy1t9cQlo0FeMLmvui1BOImYxPQRu-Ci6Y.

[44] R. Avaz, H. Nguyen, M. Malpica, and A. K. Miri, "Bioink Instability in Extrusion Bioprinting : Role of Shear Thinning," pp. 1–12.

[45] A. K. Miri, A. Khalilpour, B. Cecen, S. Maharjan, S. R. Shin, and A. Khademhosseini, "Multiscale bioprinting of vascularized models," *Biomaterials*, vol. 198, pp. 204–216, 2019.

[46] G. Hauke, *An introduction to fluid mechanics and transport phenomena*, vol. 86. Springer, 2008.

[47] J. H. Ferziger, M. Perić, and R. L. Street, *Computational methods for fluid dynamics*, vol. 3. Springer, 2002.

[48] S. Larsson and V. Thomée, *Partial differential equations with numerical methods*, vol. 45. Springer Science & Business Media, 2008.

[49] J. Blazek, *Computational fluid dynamics: principles and applications*. Butterworth-Heinemann, 2015.

[50] H. K. Versteeg and W. Malalasekera, *An introduction to computational fluid dynamics: the finite volume method*. Pearson education, 2007.

[51] R. Courant, K. Friedrichs, and H. Lewy, "Über die partiellen Differenzengleichungen der mathematischen Physik," *Math. Ann.*, vol. 100, no. 1, pp. 32–74, 1928.

[52] J. Crank and P. Nicolson, "A practical method for numerical evaluation of solutions of partial differential equations of the heat-conduction type," in *Mathematical Proceedings of the Cambridge Philosophical Society*, 1947, vol. 43, no. 1, pp. 50–67.

[53] R. W. Clough, "The finite element method in plane stress analysis," 1960.

[54] B. E. Launder and D. B. Spalding, "Mathematical models of turbulence Academic Press," *New York*, 1972.

[55] S. V. Patankar, "Heat and mass transfer in turbulent boundary layers," 1967.

[56] A. D. Gosman, *Heat and mass transfer in recirculating flows*. Academic press, 1969.

[57] C. M. Rhie and W. L. Chow, "Numerical study of the turbulent flow past an airfoil with trailing edge separation," *AIAA J.*, vol. 21, no. 11, pp. 1525–1532, 1983.

www.manaraa.com

[58] G. Falkovich, *Fluid mechanics: A short course for physicists*. Cambridge University Press, 2011.

[59] F. Moukalled, L. Mangani, and M. Darwish, *The finite volume method in computational fluid dynamics*, vol. 6. Springer, 2016.

[60] O. Reynolds, A. W. Brightmore, and W. H. Moorby, *Papers on Mechanical and Physical Subjects: The sub-mechanics of the universe*, vol. 3. The University Press, 1903.

[61] Y. Cengel and T. M. Heat, *A practical approach*. New York, NY, USA: McGraw-Hill, 2003.

[62] F. P. Incropera, D. P. Dewitt, T. L. Bergman, and A. S. Lavine, "Fundamentals of heat and mass transfer, 6th edn (trans: Xinshi G, Hong Y)." Chemistry Industry Press, Beijing (Chinese), 2007.

[63] R. B. Bird, "Transport Phenomena, ed. by RB Bird, WE Stewart and EN Lightfoot." Wiley, New York, 2006.

[64] G. Emanuel and M. Gad-El-Hak, "Analytical Fluid Dynamics," *ApMRv*, vol. 54, no. 4, p. B68, 2001.

[65] J. A. Fay, *Introduction to fluid mechanics*. MIT press, 1994.

[66] J. F. Thompson, Z. U. A. Warsi, and C. W. Mastin, *Numerical grid generation: foundations and applications*, vol. 45. North-holland Amsterdam, 1985.

[67] S.-W. Cheng, T. K. Dey, and J. Shewchuk, *Delaunay mesh generation*. CRC Press, 2012.

[68] J. F. Thompson, B. K. Soni, and N. P. Weatherill, *Handbook of grid generation*. CRC press, 1998.

[69] P. L. George, *Automatic mesh generation: applications to finite element methods*. John Wiley & Sons, Inc., 1992.

[70] P. Frey and P. L. George, "Mesh generation, vol. 32." John Wiley & Sons, 2010.

[71] M. W. Bern and P. E. Plassmann, "Mesh Generation.," *Handb. Comput. Geom.*, vol. 38, 2000.

[72] D. J. Mavriplis, "Mesh generation and adaptivity for complex geometries and flows," in *Handbook of computational fluid mechanics*, Elsevier, 1996, pp. 417–459.

[73] J. A. Chappell, J. A. Shaw, and M. Leatham, "The generation of hybrid grids incorporating prismatic regions for viscous flow calculations," Mississippi State Univ., Mississippi State, MS (United States), 1996.

[74] "Open FOAM," [Online]. Available: https://openfoam.org/.

[75] D. J. Mavriplis, "Unstructured grid techniques," *Annu. Rev. Fluid Mech.*, vol. 29, no. 1, pp. 473–514, 1997.

المنارة للاستشارات
www.manaraa.com

[76] I. ANSYS, “Fluent Theory Guide,” p. 814, 2013, [Online]. Available: http://www.pmt.usp.br/ACADEMIC/martoran/NotasModelosGrad/ANSYS Fluent Theory Guide 15.pdf.

[77] ANSYS, “Viscosity for Non-Newtonian Fluids,” *ANSYS*, p. 7, [Online]. Available: https://www.afs.enea.it/project/neptunius/docs/fluent/html/ug/node297.htm.

[78] A. K. Miri, E. Mostafavi, D. Khorsandi, S.-K. Hu, M. Malpica, and A. Khademhosseini, “Bioprinters for organs-on-chips,” *Biofabrication*, vol. 11, no. 4, p. 42002, 2019.

[79] C. J. Lovitt, T. B. Shelper, and V. M. Avery, “Advanced cell culture techniques for cancer drug discovery,” *Biology (Basel).*, vol. 3, no. 2, pp. 345–367, 2014.

www.manaraa.com